NASA-TM-86278 19840024283

NASA Technical Memorandum 86278

EXPERIENCE WITH TRANSONIC UNSTEADY AERODYNAMIC CALCULATIONS

J. W. EDWARDS, S. R. BLAND, AND D. A. SEIDEL

AUGUST 1984

National Aeronautics and
Space Administration

Langley Research Center
Hampton, Virginia 23665

EXPERIENCE WITH TRANSONIC UNSTEADY AERODYNAMIC CALCULATIONS

J. W. Edwards, S. R. Bland and D. A. Seidel
Unsteady Aerodynamics Branch
National Aeronautics and Space Administration
Langley Research Center
Hampton, Va 23665
USA

SUMMARY

Comparisons of calculated and experimental transonic unsteady pressures and airloads for four of the AGARD Two-Dimensional Aeroelastic Configurations and for a rectangular supercritical wing are presented. The two-dimensional computer code, XTRAN2L, implementing the transonic small perturbation equation was used to obtain results for: (1) pitching oscillations of the NACA 64A010A, NLR 7301 and NACA 0012 airfoils, (2) flap oscillations for the NACA 64A006 and NLR 7301 airfoils, and (3) transient ramping motions for the NACA 0012 airfoil. Results from the three-dimensional code XTRAN3S are compared with data from a rectangular supercritical wing oscillating in pitch. These cases illustrate the conditions under which the transonic inviscid small perturbation equation provides reasonable predictions.

LIST OF SYMBOLS

CT	Computational Test Case
C_p	pressure coefficient
C_p^*	critical pressure coefficient
$\bar{C}_p$	normalized unsteady pressure coefficient; first harmonic of C_p divided by oscillation amplitude in radians
$\Delta\bar{C}_p$	normalized unsteady lifting pressure coefficient, $\bar{C}_{p_\ell} - \bar{C}_{p_u}$
c	airfoil chord, m
c_ℓ	lift coefficient
c_{ℓ_α}	first harmonic lift coefficient due to pitch, per radian
c_{ℓ_δ}	first harmonic lift coefficient due to flap rotation, per radian
c_{m_α}	first harmonic pitching moment coefficient due to pitch, per radian
c_{m_δ}	first harmonic pitching moment coefficient due to flap rotation, per radian
c_{h_δ}	first harmonic hinge moment coefficient due to flap rotation, per radian
c_r	wing reference chord, m
f	oscillation frequency, Hz
LE	leading edge value
k	reduced frequency, $\omega c/2V$
ℓ	lower surface value
M	free stream Mach number
Re	Reynolds number, Vc/ν
r	airfoil function, $z = r(x,t)$ on the airfoil surface, m
TE	trailing edge value
t	time, s
u	upper surface value
V	free stream velocity, m/s
x	streamwise coordinate relative to leading edge, m
x_α	pitch axis location relative to leading edge, m
x_δ	flap axis location relative to leading edge, m
y	coordinate normal to x and z, positive to right, m
z	coordinate normal to free stream, positive up, m
α	angle of attack, deg
α_m	mean angle of attack, deg
α_0	dynamic pitch angle, deg
γ	ratio of specific heats
δ	flap angle, deg
δ_m	mean flap angle, deg
δ_0	dynamic flap angle, deg
ϵ	airfoil thickness ratio
η	fraction of semi-span
ν	kinematic viscosity, m^2/s
τ	nondimensional time in semichords traveled, $2Vt/c$
ϕ	perturbation velocity potential
ω	angular frequency, $2\pi f$, rad/s
$[\cdots]$	indicates jump in $\cdots$

All angles are positive for trailing edge down. Moments are positive nose up. Pitching moments are taken about the quarter chord except for the NLR 7301 airfoil for which they are taken about x/c = 0.4. Hinge moments are referred to the flap hinge axis located at x/c = 0.75.

1. INTRODUCTION

The field of aeroelastic response and flutter prediction has traditionally relied upon linear subsonic and supersonic unsteady aerodynamics coupled with linear descriptions of aircraft structural dynamics to perform stability analyses. In the transonic speed regime where the aerodynamic theories were not on a technically sound foundation, numerous wind tunnel tests of flutter models and flight test experience provided the confidence to operate aircraft. Due to the lack of more accurate transonic aerodynamic theory, linear unsteady airloads have been used for flutter predictions and have been reasonably successful in providng conservative flutter boundaries. Emerging aircraft designs calling for aircraft performance objectives at maneuvering flight conditions and seeking optimized aerodynamic and structural configurations press these traditional aeroelastic design tools beyond their accuracy limits. New aeroelastic response computational techniques based upon accurate simulation of the nonlinear transonic flow field are needed to bridge this gap.

The past decade has witnessed a maturing of experimental and computational capabilities aimed at filling this gap. Unsteady surface pressure measurements have been made at transonic speeds on a series of two-dimensional (2-D) and three-dimensional (3-D) wind tunnel models oscillating in several modes of motion. Tijdeman and Schippers (Ref. 1) published pressure measurements for an NACA 64A006 airfoil with an oscillating trailing-edge control surface for Mach numbers from 0.5 to 1.0. Tijdeman, (Ref. 2), provided data for the 16.5 percent thick NLR 7301 airfoil oscillating in pitch for Mach numbers between 0.5 and 0.8 and gave seminal descriptions of the characteristics of transonic unsteady aerodynamics. Davis and Malcolm (Ref. 3) tested two airfoils in pitching and plunging motions: a nominal NACA 64A010 airfoil (designated herein as NACA 64A010A) for Mach numbers up to 0.85 and an NLR 7301 airfoil for Mach numbers up to 0.808. Landon (Ref. 4) gives data for the NACA 0012 airfoil representative of a helicopter blade in dynamic stall conditions. Time-dependent results are given for large amplitude oscillatory pitching motions and for transient ramp motions. The AGARD Structures and Materials panel has selected these cases as AGARD Two-Dimensional Aeroelastic Configurations (Ref. 5). Also included in these standard configurations are the 6 percent thick parabolic arc airfoil and the MBB A-3 and DO A1 supercritical airfoils for which no experimental data sets are currently available.

Five AGARD Three-Dimensional Aeroelastic Configurations also have been selected (Ref. 6). The planforms include a rectangular unswept wing, three sweptback tapered wings and a horizontal tail model. Data from pitch oscillation tests on the NORA horizontal tail model in four European wind tunnels is presented in Ref. 7. The symmetrical sweptback RAE Wing A (Ref. 8) has been tested for both pitching and control surface oscillations. Data for the LANN supercritical transport type wing oscillating in pitch is available in Ref. 9 while some data for control surface oscillations on the ZKP wing is given in Ref. 10. A compendium describing the available data sets for the two- and three-dimensional standard configurations has been published in Ref. 11. Lambourne's general review remarks (Ref. 11) are particularly enlightening regarding the use of these data sets. Other three-dimensional unsteady pressure tests of interest include a clipped-tip delta wing with pitching and control surface oscillations (Ref. 12) and an aspect ratio 10.8 supercritical wing with oscillating control surfaces (Ref. 13). Of particular interest because of its simple geometry is the data from a rectangular supercritical wing oscillating in pitch reported by Ricketts et al. (Ref. 14).

Turning now to the computational capability of providing comparisons with these experimental data sets, the situation must be discussed in terms of algorithm development, computational expense and computer resource availability. The early results of Magnus and Yoshihara (Ref. 15) using an Euler equation code were promising but required excessive solution times on the computers available at that time. Chyu and his colleagues (Refs. 16-18) have applied an unsteady Navier-Stokes equation code for benchmark comparisons with the NACA 64A010A data of Ref. 3 at $M = 0.8$ and $\alpha_m = 0$ and 4 deg. and with the NLR 7301 data of Ref. 3 at $M = 0.74$ and $\alpha_m = 0.37$ deg. Computational expense precludes exhaustive correlation of such codes with the data sets. Also, current supercomputer memory sizes do not yet allow sufficient grid density to enable accurate three-dimensional Navier-Stokes computations. Thus most of the published comparisons of computed and experimental unsteady data has been accomplished with potential equation codes with viscous effects sometimes simulated by coupling the inviscid outer flow to a viscous boundary layer model.

Finite-difference solutions of the transonic small disturbance (TSD) potential equation were first obtained with the assumption of time linearization. This harmonic perturbation approach has been followed by Ehlers (Ref. 19) and Ehlers and Weatherill (Ref. 20). Economical solutions of the time-accurate TSD equations were enabled by the alternating-direction implicit (ADI) algorithm introduced in the LTRAN2 code by Ballhaus and Goorjian (Ref. 21). The LTRAN2 algorithm has been extensively updated with a series of improvements including: addition of time derivative terms in the boundary conditions (Houwink and van der Vooren, LTRAN2-NLR, Ref. 22), addition of ϕ_{tt} term (Rizzetta and Chin, Ref. 23 and Isogai, Ref. 24), non-reflecting far-field boundary conditions (Kwak, Ref. 25), and monotone differencing to eliminate expansion shocks (Goorjian and Van Buskirk, Ref. 26). Seidel et al. (Ref. 27) showed that the influence of the computational grid for dynamic calculations can be severe for cases with sparse grids, such as generally are used in three-dimensional calculations. The XTRAN2L code (Ref. 28) incorporates all of these features as well as a transient aeroelastic response capability. Malone (Ref. 29) gives comparisons of results from a 2-D full potential equation method with Davis' NACA 64A010A test data. Results obtained by coupling viscous boundary layer models with 2-D TSD codes are given in Refs. 30-33. Borland and Rizzetta (Ref. 34) used the ADI solution algorithm in the XTRAN3S code to obtain 3-D TSD equation solutions for isolated wings. Comparisons of calculations from the XTRAN3S code with experimental results are given by Malone and Ruo (Ref. 35), by Seidel et al. (Ref. 36) and by Guruswamy and Goorjian (Ref. 37).

The published comparisons of calculated and experimental unsteady pressures and airloads have most frequently served to verify the correctness of computational algorithm modifications and have therefore usually been of limited extent. Also, it is common to show calculations for a single test configuration. Thus it would be beneficial to have comparisons for a range of configurations in which a common computational procedure is used. This is particularly true regarding TSD calculations wherein the available approximations encompassed by the theory can account for significant differences in the calcu-

lations. This paper presents comparisons of unsteady pressures and airloads calculated by the XTRAN2L code with the available 2-D data sets for the AGARD computational test case (CT) conditions. In each of the calculations for the AGARD 2-D cases, the suggested AGARD Computational Test case conditions were used (see Ref. 11). Comparisons with test data for the NACA 64A010A, NACA 64A006, NLR 7301 and NACA 0012 airfoils are presented. Comparisons with test data for all of the AGARD CT cases for the first three of these airfoils are given in Ref. 44. In addition, sample comparisons of data from the rectangular supercritical wing (Ref. 14) with XTRAN3S calculations are given. Comments on the use of these codes for transonic unsteady aerodynamic calculations are included.

2. TRANSONIC SMALL DISTURBANCE EQUATION

2.1 Two-Dimensional Case.- All two-dimensional calculations were obtained using the XTRAN2L code (Ref. 28) which solves the complete unsteady TSD potential equation. In terms of the scaled variables used in the code, this equation is

$$(C\Phi_T + A\Phi_X)_T = (E\Phi_X + F\Phi_X^2)_X + (\Phi_Z)_Z \tag{1}$$

The NLR scaling of Ref. 24 is used to define the variables and coefficients as

$$T = \omega t \qquad \epsilon^* = \epsilon M^2(\gamma^* + 1)$$
$$X = x/c \qquad \gamma^* = 2 - (2 - \gamma)M^2$$
$$Z = z\epsilon^{*1/3}/c \qquad \Phi = \phi/(cV\epsilon^{*2/3})$$
$$C = 4k^2M^2/\epsilon^{*2/3} \qquad E = (1-M^2)/\epsilon^{*2/3}$$
$$A = 4kM^2/\epsilon^{*2/3} \qquad F = -\tfrac{1}{2}M^2(\gamma^* + 1)$$

(The reduced frequency k is based on semi-chord). The airfoil flow tangency and trailing wake conditions are applied on the z = 0 line and, in the small disturbance approximation, become

$$\Phi_Z^{\pm} = R_X^{\pm} + 2kR_T^{\pm} \quad ; \quad Z = 0^{\pm},\ 0 \le X \le 1 \tag{2a}$$

$$[\Phi_X] + 2k[\Phi_T] = 0 \quad ; \quad Z = 0,\ X > 1 \tag{2b}$$

where the ± refer to the airfoil upper or lower surfaces and $R = r\epsilon^{*1/3}/c$. The airfoil surface slopes, R_X, required in Eq. (2a) were generated by spline curve-fitting the airfoil coordinates (Ref. 5). The curve fits were performed parametrically versus surface arclength running continuously from the upper surface trailing edge around the leading edge to the lower surface trailing edge. (Spline fitting the upper and lower surfaces separately can lead to erratic results near the leading edge.) No modifications to the resulting surface slopes were made to improve correlation of small perturbation calculations with experiment, as is sometimes done.

Numerical solutions of Eq. (1) were obtained using the ADI algorithm of Rizzetta and Chin (Ref. 23) which is similar to that used in the LTRAN2 code (Ref. 21) with the addition of a three-time-level representation of the Φ_{TT} term in the Z-sweep. The monotone differencing method, first used in implicit algorithms in Ref. 26, is used to eliminate nonphysical expansion shocks. Kwak (Ref. 25) implemented far-field boundary conditions in the LTRAN2 code appropriate for the low frequency version of Eq. (1) (without the Φ_{TT} term). The corresponding conditions for the full frequency equation are given by Whitlow (Ref. 28):

upstream	$(A/B + D/B)\,\Phi_T - 2\Phi_X = 0$	(3a)
downstream	$(-A/B + D/B)\,\Phi_T + 2\Phi_X = 0$	(3b)
above (+) and below (-)	$(BD/A)\Phi_X \pm \Phi_Z = 0$	(3c)

where $B = E + 2F\Phi_X$ and $D = (4C + A^2/B)^{1/2}$.

These nonreflecting far-field boundary conditions allow the boundaries to be moved closer to the airfoil and allow greater freedom in tradeoffs among number of grid points, accuracy and expense. The default XTRAN2L grid (Ref. 27) is 80 x 61 points in x,z and covers a fixed physical extent of ±20c in x and ±25c in z. On the airfoil the x-grid has 51 grid points having a uniform spacing of 0.02c with an additional point near the leading edge. Both of these features differ from the similar LTRAN2-HI (Ref. 38) and LTRAN2-NLR (Ref. 22) codes wherein the physical grid extent varies with Mach number and thickness and covers several hundreds of chordlengths. Also, both of these codes cluster more x-grid points near the leading and trailing edges, LTRAN2-NLR having a midchord grid spacing of 0.05c and LTRAN2-HI a value of 0.03c.

Transient airloads due to pulsed airfoil motions allow complete airload frequency response functions to be calculated from a single response calculation using transfer function techniques. Of course this requires the assumption of at least local linearity of the response to the forcing function, which appears to hold widely for integrated airloads in attached flow. These features are studied in Refs. 39 and 40 which demonstrate the use of XTRAN2L in aeroelastic calculations (in Ref. 39 the code did not contain the ϕ_{tt} term). Ref. 27 uses this pulse transform technique to demonstrate key features of the relation between computational grids, boundary conditions and dynamic computations. The importance of controlling reflections of disturbances at the outer boundaries either by moving the boundary to large distances or by implementing nonreflecting boundary conditions is demonstrated. Of particular importance

are the far-field z-boundaries. Disturbances observed in the transient responses for perfectly reflecting boundaries correlate with the acoustic propagation time for travel to and return from these boundaries. These disturbances contaminate the unsteady airloads at low reduced frequencies ($k < 0.15$). The nonreflecting boundary conditions of Ref. 28 eliminate these disturbances. The option of moving the boundaries to large distances introduces the complication of grid stretching in the near-field. In this case, disturbances observed in the transient responses correlate with propagation times for travel to and return from regions of the z-grid where grid spacing first becomes more than two chordlengths. These disturbances tend to contaminate the unsteady airloads in the frequency range $0.2 < k < 1.0$. Calculations verify that these features, which are most easily studied for linearized examples, carry over to fully transonic calculations.

A warning is called for with regard to the use of potential equation codes for transonic calculations with strong shocks. Salas et al. (Ref. 40) summarize the understanding of nonunique solutions of the transonic full potential equation for these situations. Williams et al. (Ref. 42) have confirmed the existence of such solutions for the time-accurate TSD XTRAN2L code. Figure 1a shows the three upper surface solutions which may be obtained for the NACA 0012 airfoil at $M = 0.84$ and $\alpha = 0$ deg. The middle pressure distribution is a symmetric nonlifting solution while the other two are lifting solutions. Fig. 1b gives the lift coefficient at $M = 0.84$ versus mean angle-of-attack for 1) steady conditions, 2) pitching oscillation for $k = 0.01$ and 3) pitching oscillation for $k = 0.05$. The nonlifting steady case at $\alpha = 0$ deg., denoted B in the figure, is unstable and diverges with an extremely small time constant to either A or C depending upon initial conditions. At $k = 0.05$, a solution is calculated which oscillates about the positive lifting solution. The average lift curve slope of this oscillation is not unreasonable even though the underlying steady flow is anomalous. In contrast, the solution for $k = 0.01$ exhibits a hysteresis loop, jumping between the two stable steady solutions. The large phase lag implied by this solution is unphysical and caution must be exercised against such calculations.

2.2 Three-dimensional code XTRAN3S.- Three-dimensional calculations were performed with the XTRAN3S code (Refs. 34, 36) which uses a time-accurate ADI finite-difference scheme to solve the three-dimensional TSD equation

$$(C\Phi_T + A\Phi_X)_T = (E\Phi_X + F\Phi_X^2 + G\Phi_Y^2)_X + (\Phi_Y + H\Phi_X\Phi_Y)_Y + (\Phi_Z)_Z \tag{4}$$

The nondimensional variables are

$$X = x/c_r \qquad T = \bar{k}Vt/c_r$$
$$Y = y/c_r \qquad \Phi = \phi/(Vc_r)$$
$$Z = z/c_r$$

Two different sets of coefficients are provided for the TSD eq. (4). For both cases

$$C = \bar{k}^2M^2 \qquad A = 2\bar{k}M^2 \qquad E = 1-M^2$$

where $\bar{k}$ is an arbitrary scaled frequency ($\bar{k} = 1$ herein). The coefficients for the nonlinear terms may be chosen as either

$$F = -\tfrac{1}{2}(\gamma + 1)M^2 \qquad G = \tfrac{1}{2}(\gamma - 3)M^2 \qquad H = -(\gamma - 1)M^2 \tag{5}$$

or

$$F = -\tfrac{1}{2}(3 - (2 - \gamma)M^2)M^2 \qquad G = -\tfrac{1}{2}M^2 \qquad H = -M^2 \tag{6}$$

The outer boundary conditions imposed on the flow-field are

upstream	$\Phi = 0$	(7a)
downstream	$\Phi_X + \bar{k}\Phi_T = 0$	(7b)
above and below	$\Phi_Z = 0$	(7c)
spanwise and wing root	$\Phi_Y = 0$	(7d)
wake	$[\Phi_Z] = [\Phi_X + \bar{k}\Phi_T] = 0$	(7e)

The airfoil flow tangency condition is

$$\Phi_Z^{\pm} = R_X^{\pm} + \bar{k}\,R_T^{\pm} \;; \quad Z = 0^{\pm}, \quad X_{LE} \le X \le X_{TE} \tag{8}$$

where $R = r/c_r$. The code was run on a CDC CYBER 203 computer using the computational grid described in Ref. 26 with 60 x 20 x 40 points in the x, y, and z directions. The program grid size restrictions and the reflecting boundary conditions, Eq. 7, assure that disturbances reflected by the boundaries or internal grid stretching will be present. The x, z grid was chosen to minimize the effect of the internal grid reflections for $k < 0.50$ (Ref. 27). The CYBER 203 is capable of scalar or vector arithmetic. The scalar version of the XTRAN3S program required 1.9 seconds of central processor unit (CPU) time per time step. Vectorizing the ADI x-sweep and a matrix manipulation routine reduced the required time to 1.2 CPU seconds per time step.

Although both the XTRAN2L and XTRAN3S codes have provision for including quasi-steady boundary layer effects, this capability was not used, and only inviscid results are given.

3. RESULTS AND DISCUSSION

Results are given for four of the AGARD Standard Configuration airfoils and for the rectangular supercritical wing of Ref. 14. The modes of motion are described as follows. For pitch about a mean angle of attack, α_m, the total angle of attack is expressed as:

$$\alpha(t) = \alpha_m + \alpha_o \sin \omega t \tag{9}$$

where $\omega = 2kV/c$. For control surface rotation

$$\delta(t) = \delta_m + \delta_o \sin \omega t \tag{10}$$

For each case shown, the steady flow pressure distribution is plotted and compared with the measured distribution. Upper and lower surface unsteady pressures for the oscillating cases are given as the real and imaginary parts (or magnitude and phase angle) of the first harmonic component of the pressure computed from the last cycle of the imposed simple harmonic motion using a fast Fourier transform analysis. These first harmonic components are normalized by the nondimensional amplitude of motion. Tables 1-4 give the computational test (CT) cases for each of the 2-D airfoils with the priority cases indicated by an asterisk. Also noted are the figure numbers corresponding to the cases included herein (all of the CT cases have been analyzed). The reduced frequency is based on semichord. In addition to the plotted pressure distributions, the first harmonic force coefficients for all of the CT cases for the NACA 64A010A, NACA 64A006, and NLR 7301 airfoils are given in tables 5-7.

3.1 Two-Dimensional Cases. The airfoil geometry and analysis conditions were taken as the AGARD standard configurations in reference 5. For the 2-D cases calculated with XTRAN2L a steady flow field was first computed using either a steady flow algorithm or the time accurate ADI algorithm with no airfoil motion. Then the unsteady calculation was commenced using the ADI scheme. Typically, five cycles of oscillation were computed with 360 steps per cycle for the oscillatory cases. These relatively conservative conditions assured that unwanted transients had died out.

NACA 64A010A. The AGARD CT cases for this airfoil are listed in table 1. The cases are for the model tested at the NASA Ames Research Center for which experimental data are reported in Refs. 3 and 11. Note that the NACA 64A010A airfoil as tested has a small amount of camber and is 10.6 percent thick, in contrast with the 10 percent thick symmetric design section. The model had a chord of 0.5m and a tunnel height/model chord ratio of 6.7. The CT cases are for the model pitching about the quarter-chord with a zero mean angle at essentially two Mach numbers, M = 0.5 and 0.8. No transition strip was used and no wind tunnel corrections were made to the data.

Figure 2 gives the calculated and measured steady pressure distributions for M = 0.5 (CT 2) and M = 0.796 (CT 3-8). At the lower Mach number, agreement is very good with a slight overprediction of pressure over most of the chord. At the higher Mach number, the agreement is also quite good with the predicted shock location slightly aft of the measured location. Thus viscous effects appear to be relatively small for these cases.

The unsteady results are shown in figures 3-5 and table 5. At M = 0.5 (fig. 3) the agreement is excellent for both upper and lower surface for this subsonic case. Figure 4 shows the effect of frequency at M = 0.796 with k varying from 0.025 to 0.30. The calculated shock pulse occurs 5-10 percent aft of the measured position in contrast with the steady shock locations which are within two percent. A systematic decrease in calculated shock pulse width with increasing frequency is evident, with agreement of the theory and experiment perhaps being somewhat better at the intermediate frequencies. Also of note is the agreement in pressure levels and trends between the upper and lower surfaces. The effect of oscillation amplitude is illustrated in figure 5 for α_o = 0.5, 1.0, and 2.0 degrees (CT 8,5,9) at k = 0.101. With the exception of the shock pulse location, the agreement with the experiment is good and the effect of amplitude on the shock pulse is well illustrated by the theory. Away from the shock, the plotted normalized pressures are essentially independent of amplitude. However, for smaller amplitudes, the shock pulse is narrower (less shock motion) and higher (because of the amplitude normalization).

Figure 6 summarizes the integrated lift and moment coefficient data for M = 0.796 (table 5). The LTRAN2-NLR inviscid and the LTRANV viscous results reported in Ref. 32 are included for reference. The agreement shown between the XTRAN2L and LTRAN2-NLR results is noteworthy since they are obtained from significantly different computational codes. The inviscid results deviate from experiment at the lowest frequencies but otherwise show proper trends with increasing frequency. With the exception of $\mathrm{Im}(c_{\ell_\alpha})$ the LTRANV viscous corrections improve the agreement with experiment. The $\mathrm{Im}(c_{\ell_\alpha})$ correction is unnecessary at k = 0.1 and has the wrong sign at k = 0.2.

NACA 64A006. The AGARD test cases for this airfoil are listed in table 2 and are for the model tested at the NLR. The test cases all involve oscillation about zero mean angle of a flap with hinge axis located at three-quarter-chord. The variations include five Mach numbers, two frequencies, and two oscillation amplitudes. Experimental data are given in Refs. 1 and 11. The model had a chord of 0.18m and a tunnel height/model chord ratio of 3.1. Transition was fixed at 0.1c and no wind tunnel corrections were made to the data.

The steady flow pressure distributions for Mach numbers from 0.80 to 0.875 are shown in figure 7. Figures 8 and 9 shown the unsteady upper surface pressures at each Mach number for frequencies near k = 0.06 and 0.24 respectively. In general, the agreement between experiment and theory improves with decreasing Mach number and increasing frequency. The steady flow comparisons (fig. 7) are very good at subcritical Mach numbers, but deteriorate as the shock wave develops. For unsteady flow, figures 8 and 9 illustrate the better agreement between theory and experiment that occurs at higher frequency for all Mach numbers. This is particularly true of the surface pressures forward of the shock pulse. Unsteady pressures on the control surface, aft of x/c = 0.75, are well predicted at all conditions except the imaginary part for the low frequency case at M = 0.875. For both frequencies, as the Mach number increases, the calculated shock pulse moves aft and interacts with the pressure pulse at the hinge location. The experimental shock pulse is 10-15 percent further forward than the calculated pulse at

M = 0.875. At this Mach number, the experimental shock peak (near x/c = 0.55) and the hinge peak (x/c = 0.75) are easily distinguished. In the calculations the two peaks have merged into one at the lower frequency (fig. 8) but can be identified at the higher frequency (fig. 9). This result is not surprising since the shock excursion is expected to decrease as frequency increases.

Figures 10-11 show the integrated lift, moment and hinge moment coefficient data for these cases (table 6). Again the LTRAN2-NLR inviscid and LTRANV viscous results from Ref. 32 are included for comparison. As for the NACA 64A010A airfoil, the airloads calculated by XTRAN2L and LTRAN2-NLR compare very well with each other for all Mach numbers and frequencies. At k = 0.24 the calculated XTRAN2L loads compare favorably with experiment in magnitude and in the trend with Mach number. This agreement deteriorates at the lower frequency, and is worst at the higher Mach numbers. The viscous corrections of LTRANV (Ref. 32) generally improve agreement with experiment, particularly at the higher frequency (fig. 11).

NLR 7301. The test cases for this 16.5 percent thick supercritical airfoil are listed in table 3. The experimental data are taken from the tests at the NLR. They were chosen for comparison instead of those from the NASA Ames Research Center (Chapter 5 of Ref. 11 and Ref. 3) because the model matched the design airfoil more closely, and data were available for both upper and lower surfaces. The calculated harmonic forces are given in table 7. Cases 1-9 (table 3) are for pitch oscillation about an axis located at 40 percent chord and include variations in frequency and amplitude of motion. Cases 10-14 are for oscillation of a flap located at three-quarter chord with variations in frequency at the design point. These two different modes of motion were achieved with separate wind tunnel models, designed to have identical profiles. The models had a chord of 0.18m and a tunnel height/model chord ratio of 3.1. The tests encompassed conditions with free transition and conditions with transition strips located at 0.07c and 0.3c (Table 4.4 of Ref. 11). Futhermore, the CT case conditions (Ref. 5) include steady wind tunnel interference corrections (table 0.2 and section 9.6 of Data Set 4 of Ref. 11).

Three mean flow conditions were analyzed: a subcritical condition at M = 0.5 (CT 1,2); a supercritical case with shock at M = 0.7, α_m = 2.0 deg. (CT 4); and the design point at M = 0.721, α_m = -0.19 deg. (CT 6,12). The steady flow pressures for the three mean flow conditions are shown in figure 12. At the subcritical condition, M = 0.5, the upper surface pressures are in good agreement, but the pressures on the lower surface show a discrepancy in level. It would not be surprising if small disturbance theory were inadequate for this 16.5 percent thick, blunt nosed airfoil. The comparison for the case with the strong shock, M = 0.7, is poor, with the calculation giving a shock that is too strong and located too far aft. The same overprediction of pressure on the lower surface which was seen at M = 0.5 is present while the upper surface pressure level near the leading edge is well predicted. With this degree of mismatch between the predicted and measured steady pressures no unsteady pressures are included for this case. The comparison of the steady pressure distributions at the design point (M = 0.721) are also poor. The predicted pressures show two weak shocks at about x/c = 0.25 and 0.60. In addition, there is a sharp pressure rise near the leading edge on the upper surface. One may anticipate that these features will lead to several shock pressure pulses in the unsteady results described below. Also of note are the differing steady pressures on the two models, cases CT 6 and CT 12, although the models were designed to have the same shape and were tested at the same conditions. The model with the trailing edge flap (CT 12) shows a gradual pressure rise on its upper surface with no evidence of a shock. Note that for the three mean flow conditions analyzed, a uniform trend of overprediction of lower surface pressures is observed.

The calculated unsteady results for M = 0.5 shown for pitching oscillations at two frequencies in fig. 13 agree well with the experimental data. Figures 14 and 15 give the comparisons at the design point for the model oscillating in pitch and the model with the oscillating flap. The oscillation frequency is k = 0.068 in both cases. In fig. 14 a large shock pulse is calculated on the upper surface at 0.20c with smaller pulses at 0.45c and 0.60c while the experimental shock pulses occur at 0.50c and 0.65c. The oscillating flap case, fig. 15, shows similar effects. On the upper surface, calculated shock pulses are seen at 0.20c, 0.40c and 0.65c whereas a broad experimental pulse is seen near 0.50c. A lower surface shock pulse at 0.45c is seen in the experimental data due to the critical steady pressure value at that point (fig. 12, CT 12). Note in fig. 15 that the pressure peaks due to flap motions at 0.75c are overpredicted on both the upper and lower surfaces and that the real part of the upper surface experimental pressure does not tend to zero at the trailing edge. Similar effects were seen for CT 14 where k = 0.453 (not shown). Compare these features with figs. 8 and 9 where the pressure peaks on the NACA 64A006 airfoil are well predicted at k = 0.06 and slightly underpredicted at k = 0.24.

NACA 0012. The final AGARD case for which 2-D data is available is this 12 percent thick symmetrical airfoil tested with free transition for sizable mean angles and oscillation amplitudes (CT 1-5, table 4) as well as cases with transient angle-of-attack changes at nominally constant pitch rates (CT 6-8, table 4). The model had a chord length of 0.1016m and a tunnel height/model chord ratio of 4.5. This model is unique in that its test conditions matched the full scale Reynolds numbers of helicopter blades of which it is representative. In Ref. 11 the experiemental quantities α, α_m, α_0, c_ℓ, and c_m (but not C_p) were corrected for wind tunnel interference effects. The corrections were applied to each instantaneous condition as if it were steady (Data set 3 of Ref. 11).

Results for the priority case CT 8 in which the angle-of-attack increases from 0 to 15 deg. in 42.3 semi-chordlengths at M = 0.60 are given in figure 16. Instantaneous pressures are shown for α = 0, 5.67, 8.54 and 11.62 deg. At α = 0 deg. the calculated starting (steady) pressures are below the experimental values in the leading edge region. Comparison of the similar subsonic cases for the 6 percent thick NACA 64A006 at M = 0.80 and α = 0 deg, fig. 7, and the 10.6 percent thick NACA 64A010A at M = 0.5 and α = 0 deg., fig. 2 does not show a consistent trend. The comparison of surface pressures as the angle-of-attack increases to 5.67 and 8.54 deg. is good considering the large value of α. At α = 8.54 deg. the calculated shock is sharper than the experimental. At 11.62 deg. the experimental pressures indicate a leading edge flow separation which cannot be treated by the calculations. Figure 17 compares the experimental and calculated lift coefficients versus angle-of-attack for this case, CT 8, and also for CT 7, for which the rate of change of α is decreased by one-third (0-15 deg. in 133.3 semi-chordlengths). The experimental results show that stall occurs at α = 7 deg for CT 7 where c_ℓ = 1.0 and at α = 9 deg. with

c_ℓ = 1.1 for CT 8. The calculations are able to match the experimental lift coefficients very well up to the stall angle-of-attack for these dynamic cases.

Figure 18 presents comparisons of lift and moment coefficients versus α for the oscillatory cases CT 1,2,3 and 5. The first three cases are for oscillations of α_0 = 2.5 and 5 deg. about non-zero mean angles while the last case is for oscillations of α_0 = 2.5 deg. about a zero mean angle. Agreement for the lift coefficients varies from very good to good. In contrast, the moment coefficients for fig. 18a-c show a systematic difference between the calculated and experimental values which is due in large part to the underprediction of pressures on the upper surface near the leading edge discussed above. The characteristic shape of the c_m - α curves is caused by a large second harmonic contribution. In fig. 18d, the different shape of the c_m - α curve is due to increased amplitude of the third harmonic component. These examples demonstrate the ability of the TSP code XTRAN2L to predict with reasonable accuracy airloads due to large amplitude airfoil motions within the limits of attached flow.

3.2 Three-Dimensional Case

Rectangular Supercritical Wing. Results from tests of this 12 percent thick supercritical wing are reported by Ricketts et al. (Ref. 14) and Seidel et al. (Ref. 36). The unswept wing had a 2 foot chord and a panel aspect ratio of 2.0. The design Mach number was 0.80 with a design lift coefficent of 0.60. The model was oscillated in pitch about an axis at 0.46c. The model was tested over a range of Mach number from 0.40 to 0.90 and for angles-of-attack from -1 to +7 degrees in freon. Oscillation frequencies were 5, 10, 15 and 20 Hz. This model provides a good calibration test of the 3-D TSP equation XTRAN3S code due to its moderate thickness and simple planform geometry.

Comparisons of steady pressure distributions are shown in figure 19 for Mach numbers of 0.70 and 0.825 at α = 2 degrees. Calculations are shown for both sets of coefficients, Eqs. 5 and 6. Agreement at the lower Mach number, fig. 19a, is generally good over the mid portion of the chord but with some deviation near the nose and lower trailing edge regions. There is little difference in the results obtained using the different coefficient sets except near the weak shock near the leading edge. The Eq. 6 coefficients give a somewhat stronger shock for this case. Some of the lack of agreement in the nose area may be the result of using a relatively coarse grid near the nose.

For M = 0.825, fig. 19b, the shock is further aft on the inboard portion of the wing and approaches the leading edge at the tip, showing a large three-dimensional effect. The comparison between experimental and calculated results shows trends similar to the results for M = 0.70 but with significantly poorer agreement. The coefficients of Eq. 6 give a shock that is significantly stronger and located further aft than that predicted by the coefficients of Eq. 5. Neither calculation captures the inboard shock detail (near x/c = 0.60 for η = 0.31). The comparison of pressure levels on the upper surface ahead of the shock is good. On the lower surface, agreement of presures for both fig. 19a and b is reasonably good with the same tendency for overprediction of pressure noted for the NLR 7301 airfoil (fig. 12).

Comparisons of unsteady results at M = 0.70 are shown in fig. 20. The coefficients of Eq. 6 are used and linear theory results from the RHOIV computer program (Ref. 43) are included for reference. In fig. 20a, α_0 = 1 deg, k = 0.178 and results are presented in terms of magnitude and phase of the lifting pressure coefficient. The pressure amplitudes calculated by XTRAN3S are in good agreement with the experimental data over most of the wing with some overprediction in the inboard leading edge region and underprediction over the outboard portion of the wing. The linear theory results are in good agreement with experiment except near the leading edge where transonic effects are evident. As for the pressure amplitude, the XTRAN3S results for phase show an overprediction in the inboard leading edge region. The large change in the phase data near 0.60c is due to lower surface pressures and is probably caused by viscous effects. The linear theory results for phase are in good agreement with experiment over the forward part of the airfoil. The best agreement between XTRAN3S and experiment occurs in the mid-span region where the dynamic shock is not overpredicted and the tip effects are not pronounced. Similar results are shown in fig. 20b for k = 0.356. The comparison with XTRAN3S is improved for this higher reduced frequency, particularly in the phase near the trailing edge. The linear theory pressure amplitude prediction is not as good as in fig. 20a, underpredicting the pressure near the leading edge and overpredicting the pressure near the trailing edge. Better grid resolution should lead to improvements in these predictions, particularly for the leading edge pressure peak feature of figs. 19a and 20a. Also, viscous boundary layer modeling should improve the ability to capture the upper surface shock of fig. 19b and lead to better agreement of the lower surface phase results shown in fig. 20.

4. CONCLUDING REMARKS

Comparisons of experimental unsteady pressures with calculations from transonic small disturbance theory have been presented for four of the AGARD Two-Dimensional Aeroelastic Configurations and for a rectangular wing. Results for NACA 64A010A and NLR 7301 airfoils oscillating in pitch and for NACA 64A006 and NLR 7301 airfoils with oscillating flaps have been presented. In addition, large amplitude oscillations and transient ramping motions through stall are given for the NACA 0012 airfoil. Three-dimensional results for an unswept rectangular supercritical wing oscillating in pitch are given. The cases presented cover a wide range of test conditions including subcritical flow cases and cases showing variations in Mach number, reduced frequency, and amplitude of motion. The comparisons with calculations from computer codes implementing solutions of the inviscid transonic small disturbance equation help to delineate the conditions under which this equation provides reasonable predictions. Conditions under which viscous effects need to be treated and conditions under which the small disturbance assumption is questionable are discussed.

The two-dimensional calculations are from the XTRAN2L computer code while the three-dimensional results were obtained with the XTRAN3S code. The XTRAN2L code gives very good predictions for symmetric nonlifting airfoils in subcritical flows as shown by the results for the NACA 64A010A and NACA 64A006

airfoils. For lifting cases, both codes tend to overpredict lower surface steady pressures at both subsonic and transonic conditions (NLR 7301 airfoil and supercritical wing). For the moderate transonic conditions of the NACA 64A010A calculations, pressure levels and trends were very well predicted (except for the lowest reduced frequencies) over the range of reduced frequencies from 0.025 to 0.30 and for oscillation amplitudes from 0.5 to 2.0 degrees. Viscous effects were more noticeable for the NACA 64A006 airfoil with calculated shock pulses being too far aft. Comparisons of integrated airloads for this airfoil improve significantly with increasing reduced frequency.

The NLR 7301 results illustrate the requirement of treating viscous effects. The inviscid results for this airfoil do not adequately define the shock locations, although the reasonable pressure levels give some promise of the ability of small disturbance theory coupled with viscous corrections to treat such cases. The large amplitude oscillation and transient response cases for the NACA 0012 airfoil illustrate the ability of the small disturbance theory to give reasonable unsteady calculations at conditions approaching dynamic stall.

Finally, the XTRAN3S results for the rectangular supercritical wing hold promise for the utility of transonic small perturbation equation codes for aeroelastic applications. Again, pressure levels are reasonably predicted and the agreement between calculations and experiment improves with increasing frequency. With the incorporation of more adequate computational grids and viscous modeling, significant improvements in unsteady airload predictions may be anticipated.

REFERENCES

1. Tijdeman, H. and Schippers, P., "Results of Pressure Measurements on an Airfoil with Oscillating Flap in Two-Dimensional Subsonic and Transonic Flow," NLR TR-73078U, National Aerospace Laboratory, The Netherlands, July, 13, 1973.

2. Tijdeman, H., "Investigations of the Transonic Flow Around Oscillating Airfoils," NLR TR 77090U, 1977.

3. Davis, S. S. and Malcolm, G. N., "Experimental Unsteady Aerodynamics of Conventional and Supercritical Airfoils," NASA TM 81221, August 1980.

4. Landon, R. H., "A Description of the ARA 2-Dimensional Pitch and Heave Rig and Some Results from the NACA 0012 Wing," ARA Memo No. 199, September 1977.

5. Bland, S. R., "AGARD Two-Dimensional Aeroelastic Configurations," AGARD AR 156, August 1979.

6. Bland, S. R., "AGARD Three-Dimensional Aeroelastic Configurations," AGARD AR 167, March 1982.

7. Lambourne, N.; Destuynder, R.; Kienappel, K., and Roos, R., "Comparative Measurements in Four European Wind Tunnels of the Unsteady Pressures on an Oscillating Model (the NORA Experiments), AGARD R-673, October 1979.

8. McOwat, D. M.; Welsh, B. L., and Cripps, B. E., "Time-Dependent Pressure Measurements on a Swept Wing with an Oscillating Trailing-Edge Flap," RAE Technical Report 81033 (1981).

9. Horsten, J. J.; den Boer, R. G.; and Zwaan, R. J.; "Unsteady Transonic Pressure Measurements on a Semispan Wind Tunnel Model of a Transport-Type Supercritical Wing (LANN Model). Part I: General description, Aerodynamic Coefficients and Vibration Modes," AFWAL-TR-83-3039 Part I, March 1983.

10. Couston, M.; Angelini, J. J.; and Meurzec, J. L., "Comparison of Computed and Measured Unsteady Pressure Fields on a Supercritical Wing," ONERA TP No. 12 (1981).

11. Anon., "Compendium of Unsteady Aerodynamic Measurements," AGARD R-702, August 1982.

12. Hess, R. W.; Wynne, E. C.; and Cazier, F. W., Jr., "Static and Unsteady Pressure Measurements on a 50-Degree Clipped Delta Wing at M = 0.9," AIAA Paper No. 82-0686, May 1982.

13. Sandford, M. C.; Ricketts, R. H.; Cazier, F. W., Jr., and Cunningham, H. J., "Transonic Unsteady Airloads on an Energy Efficient Transport Wing with Oscillating Control Surfaces," J. of Aircraft, Vol. 18, July 1981, pp. 557-561.

14. Ricketts, R. H.; Sandford, M. C.; Seidel, D. A.; and Watson, J. J., "Transonic Pressure Distributions on a Rectangular Supercritical Wing Oscillating in Pitch," AIAA Paper No. 83-0923, May 1983.

15. Magnus, R. and Yoshihara, H., "The Transonic Oscillating Flap," AIAA Paper No. 76-327, AIAA Fluid and Plasma Dynamics Conference, July 1976.

16. Chyu, W. J.; Davis, S. S., and Chang, K. S., "Calculation of Unsteady Transonic Flow over an Airfoil," AIAA Journal, Vol. 19, June 1981, pp. 684-690.

17. Chyu, W. J. and Kuwahara, K., "Computations of Transonic Flow Over an Oscillating Airfoil with Shock-Induced Separation," AIAA Paper No. 82-0350, AIAA Aerospace Sciences Meeting, January 1982.

18. Chyu, W. J. and Ono, K., "Unsteady Transonic Flow Over Conventional and Supercritical Airfoils," AIAA Paper No. 83-0235, AIAA Aerospace Sciences Meeting, January 1983.

19. Ehlers, F. E., "A Finite Difference Method for the Solution of the Transonic Flow Around Harmonically Oscillating Airfoils," NASA CR-2257, January 1974.

20. Ehlers, F. E. and Weatherill, W. H., "A Harmonic Analysis Method for Unsteady Transonic Flow and Its Application to the Flutter of Airfoils," NASA CR 3537, May 1982.

21. Ballhaus, W. F. and Goorjian, P. M., "Implicit Finite-Difference Computations of Unsteady Transonic Flows about Airfoils," AIAA Journal, Vol. 15, December 1977, pp. 1728-1735.

22. Houwink, R. and van der Vooren, J., "Improved Version of LTRAN2 for Unsteady Transonic Flow Computations," AIAA Journal, Vol. 18, no. 8, 1980, pp. 1008-1010.

23. Rizzetta, D. P. and Chin, W. C., "Effect of Frequency in Unsteady Transonic Flow," AIAA Journal, vol. 17, July 1979, pp. 779-781.

24. Isogai, K., "Numerical Study of Transonic Flutter of a Two-Dimensional Airfoil," NAL TR-617T, National Aerospace Laboratory, Tokyo, July 1980.

25. Kwak, D., "Non-Reflecting Far-Field Boundary Conditions for Unsteady Transonic Flow Computation," AIAA Journal, Vol. 19, November 1981, pp. 1401-1407.

26. Goorjian, P. M. and van Buskirk, R.,"Implicit Calculations of Transonic Flows Using Monotone Methods," AIAA Paper No. 81-0331, AIAA Aerospace Sciences Meeting, January 1981.

27. Seidel, D. A., Bennett, R. M. and Whitlow, W., Jr., "An Exploratory Study of Finite Difference Grids for Transonic Unsteady Aerodynamics," AIAA Paper No. 83-0503, AIAA Aerospace Sciences Meeting, January 1983.

28. Whitlow, W., Jr, "XTRAN2L: A Program for Solving the General-Frequency Unsteady Transonic Small Disturbance Equation," NASA TM 85723, November 1983.

29. Malone, J. B. and Sankar, N. L., "Numerical Simulation of 2-D Unsteady Transonic Flow using the Full-Potential Equation," AIAA Paper no. 83-0233, AIAA Aerospace Sciences Meeting, January 1983.

30. Couston, M.; Angelini, J. J.; LeBalleur, J. C. and Girodroux-Lavigne, P., "Prise en Compte d'effets de Couche Limite Instationnaire dans un Calcul Bidimensinnel Transsonique," AGARD CP-296, paper no. 6, February 1981.

31. Rizzetta, D. P., "Procedures for the Computation of Unsteady Transonic Flows Inlcuding Viscous Effects," NASA CR 166249, January 1982.

32. Houwink, R., "Unsteady Transonic Flow Computations for AGARD 2-D Aeroelastic Configurations," NLR Memo AE-83-004 U, National Aerospace Laboratory, the Netherlands, March 1983.

33. Guruswamy, P. and Goorjian, P. M., "Effects of Viscosity on Transonic-Aerodynamic and Aeroelastic Characteristics of Oscillating Airfoils," AIAA Paper no. 83-0888, AIAA Structures, Structural Dynamics and Materials Conference, May 1983.

34. Rizzetta, D. P. and Borland, C. J., "Unsteady Transonic Flow over Wings Including Viscous/Inviscid Interaction," AIAA Journal, Vol. 21, March 1983, pp. 363-371.

35. Malone, J. B. and Ruo, S. Y., "LANN Wing Test Program: Acquisition and Applicationof Unsteady Transonic Data for Evaluation of Three-Dimensional Computational Methods," AFWAL-TR-83-3006, February 1983.

36. Seidel, D. A., Bennett, R. M., and Ricketts, R. H., "Some Recent Applications of XTRAN3S," AIAA Paper No. 83-1811, AIAA Applied Aerodynamics Conference, July 1983.

37. Guruswamy, P. and Goorjian, P. M., "An Efficient Coordinate Transformation Technique for Unsteady, Transonic Aerodynamic Analysis of Low Aspect-Ratio Wings" AIAA Paper No. 84-0872, AIAA Structures, Structural Dynamics and Materials Conference, May 1984.

38. Hessenius, K. A. and Goorjian, P. M., "Validation of LTRAN2-HI by Comparison with Unsteady Transonic Experiment," AIAA Journal, Vol. 20, May 1982, pp. 731-732.

39. Edwards, J. W.; Bennett, R. M.; Whitlow, W., Jr.; and Seidel, D. A., "Time-Marching Transonic Flutter Solutions Including Angle-of-Attack Effects," J. of Aircraft, Vol. 20, November 1983, pp. 899-906.

40. Bland, S. R. and Edwards, J. W., "Airfoil Shape and Thickness Effects on Transonic Airloads and Flutter," J. of Aircraft, Vol. 21, March 1984, pp. 209-217.

41. Salas, M. D., Gumbert, C. R. and Turkel, E., "Nonunique Solutions to the Transonic Potential Flow Equation," AIAA Journal, Vol. 22, January 1984, pp. 145-146.

42. Williams, Marc H., Bland, Samuel R.; and Edwards, John W., "Flow Instabilities in Transonic Small Disturbance Theory," NASA TM 86251, 1984.

43. Redman, M. C.; and Rowe, W. S., "Prediction of Unsteady Aerodynamic Loadings Caused by Leading Edge and Trailing Edge Control Surface Motions in Subsonic Compressible Flow -- Computer Program Description," NASA CR 132634, May 1975.

44. Bland, S. R.; and Seidel, D. A., "Calculation of Unsteady Aerodynamics for Four AGARD Standard Aeroelastic Configurations," NASA TM 85817, May 1984.

Table 1. - NACA 64A010A Airfoil, Computational Test Cases

Case	M	ReX10^{-6}	α_o	f	k	Figure
1	0.490	2.5	0.96	10.4	0.100	
2	0.502	10.0	1.02	10.8	0.100	2,3
3	0.796	12.5	1.03	4.2	0.025	2,4
4	0.796	12.5	1.02	8.6	0.051	2,4
5	0.796	12.5	1.02	17.2	0.101	2,4,5
6*	0.796	12.5	1.01	34.4	0.202	2,4
7	0.796	12.5	0.99	51.5	0.303	2,4
8	0.796	12.5	0.51	17.1	0.101	2,5
9	0.797	12.5	2.00	17.2	0.101	5
10*	0.802	3.4	0.94	33.2	0.200	

Note: $\alpha_m = 0$, $x_\alpha/c = 0.25$

Table 2. - NACA 64A006 Airfoil, Computational Test Cases

Case	M	δ_o	f	k	Figure
1	0.800	1	30	0.064	7,8
2	0.800	1	120	0.254	7,9
3	0.825	1	30	0.062	7,8
4	0.825	2	30	0.062	
5	0.825	1	120	0.248	7,9
6	0.850	1	30	0.060	7,8
7	0.850	1	120	0.242	7,9
8*	0.875	1	30	0.059	7,8
9*	0.875	2	30	0.059	
10*	0.875	1	120	0.235	7,9
11	0.960	1	30	0.054	
12	0.960	1	120	0.217	

Note: $\alpha_m = \alpha_o = \delta_m = 0$, $x_\delta/c = 0.75$

Table 3. - NLR 7301 Airfoil, Computational Test Cases

Case	M	α_m	α_o	δ_o	f	k	Figure
1	0.500	0.40	0.5	0	30	0.098	12, 13a
2	0.500	0.40	0.5	0	80	0.263	12, 13b
3	0.700	2.00	0.5	0	30	0.072	
4	0.700	2.00	1.0	0	30	0.072	12
5	0.700	2.00	0.5	0	80	0.192	
6	0.721	-0.19	0.5	0	30	0.068	12, 14
7	0.721	-0.19	1.0	0	30	0.068	
8*	0.721	-0.19	0.5	0	80	0.181	
9	0.721	-0.19	0.5	0	200	0.453	
10	0.500	0.40	0	1	30	0.098	
11	0.700	2.00	0	1	30	0.072	
12	0.721	-0.19	0	1	30	0.068	12, 15
13*	0.721	-0.19	0	1	80	0.181	
14	0.721	-0.19	0	1	200	0.453	

Note: $x_\alpha/c = 0.4$, $x_\delta/c = 0.75$, $\delta_m = 0$

Table 4. - NACA 0012, Computational Test Cases

Case	M	V	ReX10^{-6}	α_m	α_o	α'	f	k	Figure
1*	0.601	197	4.8	2.89	2.41	NA	50	0.081	18
2	0.599	197	4.8	3.16	4.59	NA	50	0.081	18
3	0.599	197	4.8	4.86	2.44	NA	50	0.081	18
4	0.755	243	5.5	0.02	≈0	NA	62	0.081	
5	0.755	243	5.5	0.02	2.51	NA	62	0.081	18
6	0.292	96	2.6	NA	0→15	0.83	NA	NA	
7	0.600	191	4.6	NA	0→10	0.11	NA	NA	17
8*	0.606	194	4.7	NA	0→10	0.38	NA	NA	16,17

Note: x /c = 0.25, final α' is given.

Table 5. - NACA 64A010A Airfoil, harmonic forces

	c_{ℓ_α}		c_{m_α}	
Case	Real	Imag	Real	Imag
1	5.767	-0.561	-0.052	-0.186
2	5.802	-0.581	-0.054	-0.189
3	12.552	-4.202	-0.903	0.169
4	9.836	-4.092	-0.709	0.039
5	7.342	-3.446	-0.600	-0.160
6*	5.635	-2.157	-0.648	-0.472
7	4.942	-1.341	-0.793	-0.631
8	7.370	-3.384	-0.583	-0.195
9	7.247	-3.713	-0.674	-0.014
10*	5.496	-2.421	-0.744	-0.310

Table 6. - NACA 64A006 Airfoil, harmonic forces

	c_{ℓ_δ}		c_{m_δ}		c_{h_δ}	
Case	Real	Imag	Real	Imag	Real	Imag
1	4.793	-2.053	-1.248	-0.052	-0.082	-0.003
2	2.546	-1.744	-1.368	0.024	-0.082	-0.024
3	4.986	-2.459	-1.383	-0.043	-0.083	-0.005
4	5.006	-2.520	-1.405	-0.036	-0.082	-0.005
5	2.336	-1.968	-1.526	0.172	-0.087	-0.026
6	5.148	-3.434	-1.703	0.103	-0.080	-0.013
7	1.672	-1.891	-1.460	0.685	-0.100	-0.030
8*	3.568	-5.687	-2.079	1.655	-0.072	-0.071
9*	3.493	-5.726	-2.062	1.835	-0.111	0.010
10*	1.699	-1.372	-0.902	0.644	-0.111	-0.024
11	1.555	0.025	-0.963	-0.013	-0.190	-0.002
12	1.537	-0.004	-0.956	0.004	-0.188	0.001

Table 7. - NLR 7301 Airfoil, harmonic forces

	c_{ℓ_α}		c_{m_α}		c_{h_α}	
Case	Real	Imag	Real	Imag	Real	Imag
1	5.860	-0.792	0.842	-0.311	-0.030	-0.009
2	4.771	0.045	0.684	-0.504	-0.024	-0.032
3	8.280	-8.584	-0.320	0.751	0.028	-0.121
4	8.067	-8.867	-0.343	0.935	0.025	-0.124
5	4.697	-3.547	0.152	0.232	-0.025	-0.087
6	8.535	-2.839	1.364	-0.860	-0.022	-0.011
7	8.604	-3.048	1.272	-0.842	-0.020	-0.013
8*	6.104	-1.948	0.758	-1.122	-0.021	-0.030
9	4.808	-0.555	-0.112	-1.078	-0.021	-0.079

	c_{ℓ_δ}		c_{m_δ}		c_{h_δ}	
Case	Real	Imag	Real	Imag	Real	Imag
10	3.537	-0.787	-0.238	-0.190	-0.061	-0.005
11	4.022	-4.348	-0.873	0.399	-0.046	-0.059
12	4.989	-2.164	-0.412	-0.478	-0.057	-0.009
13*	3.139	-2.038	-0.867	-0.382	-0.059	-0.022
14	1.830	-1.056	-0.747	0.068	-0.072	-0.043

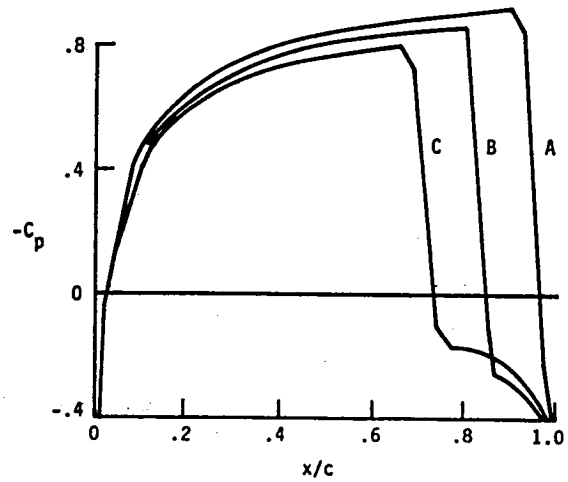

(a) Upper surface pressure distribution.

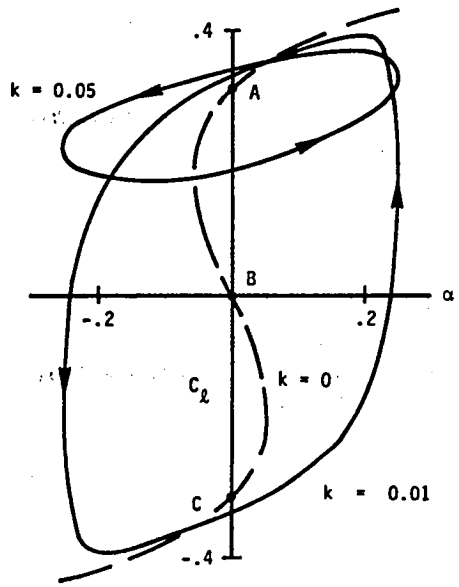

(b) Unsteady lift coefficient.

Figure 1. - Anomalous behavior of potential flow solutions for NACA 0012 airfoil at M = 0.85, α_m = 0.

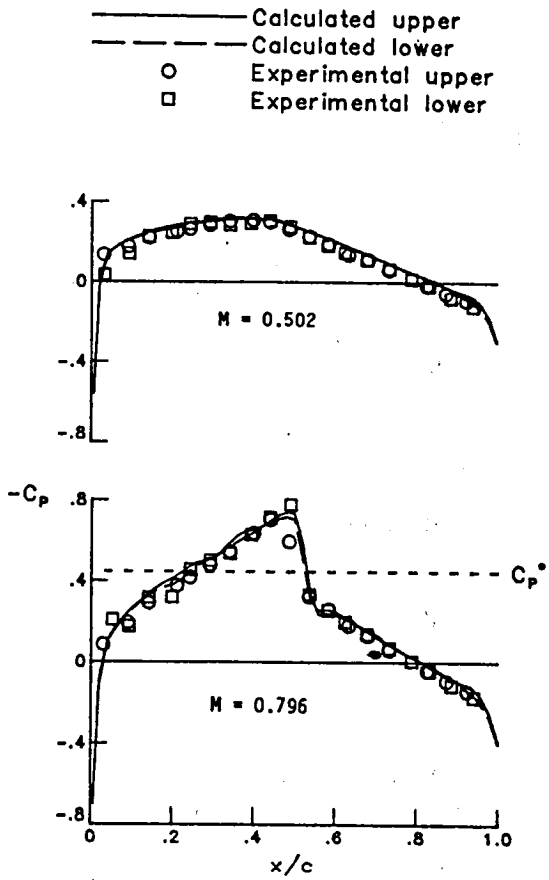

Figure 2. - Steady pressure distributions for the NACA 64A010A airfoil at $\alpha_m = 0^o$, Re = 10 x 10^6 (CT 2, 3-8).

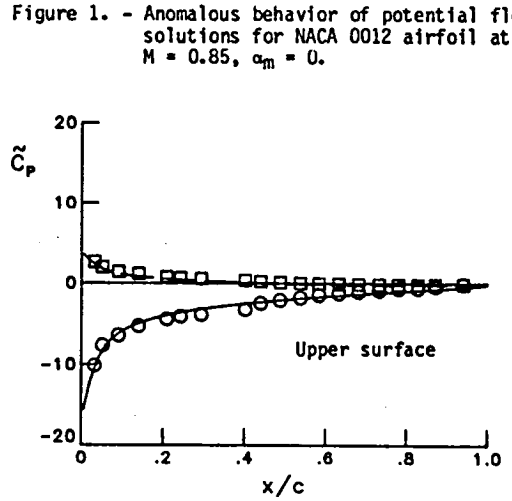

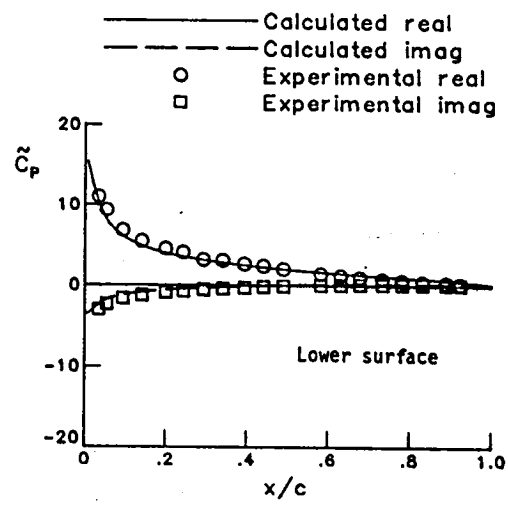

Figure 3. - Unsteady pressure distributions for the NACA 64A010A airfoil at M = 0.5, $\alpha_0 = 1^o$, k = 0.1 (CT 2).

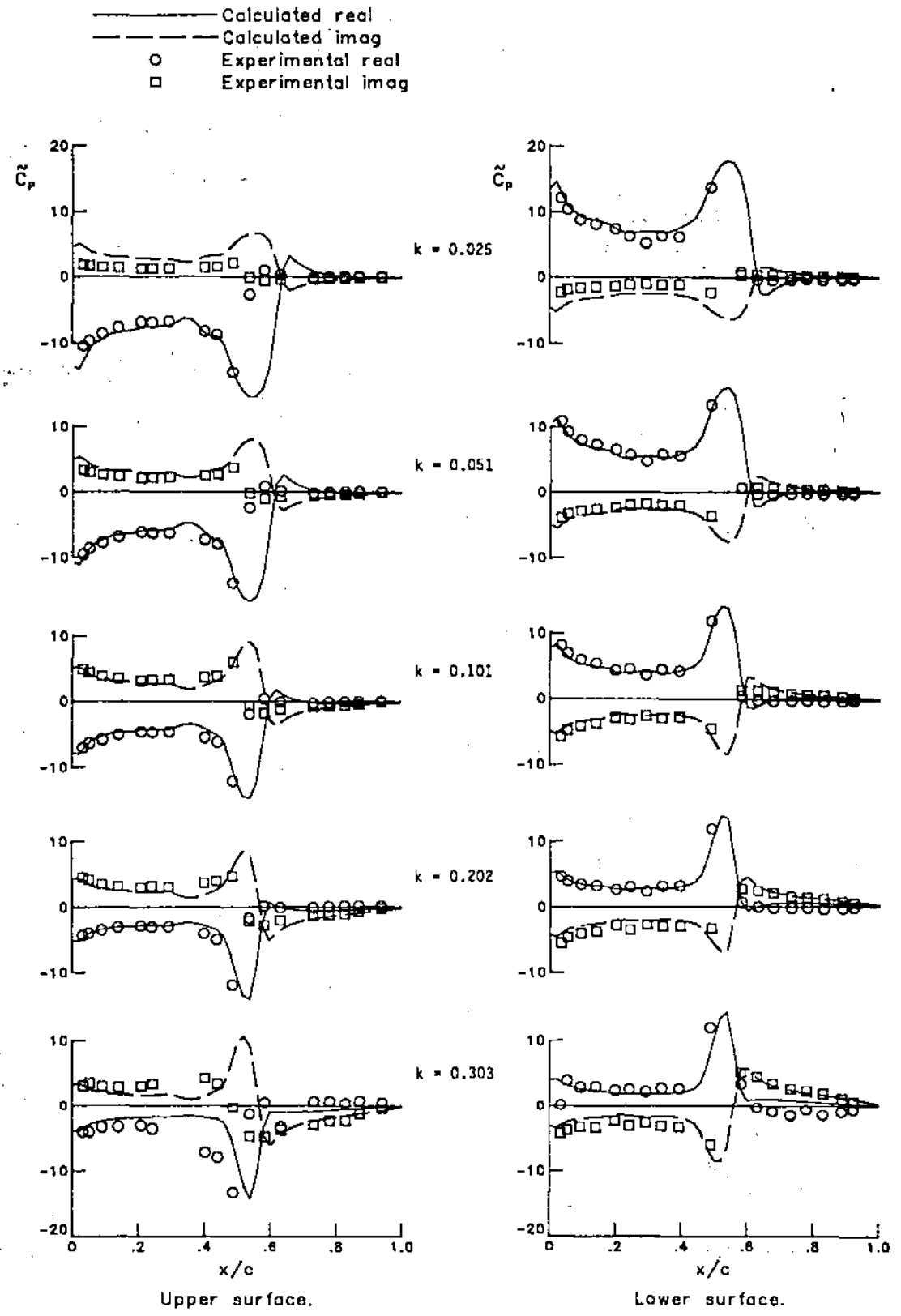

Figure 4. - Unsteady pressure distributions for the NACA 64A010A airfoil at M = 0.796, α_0 = 1° (CT 3-7).

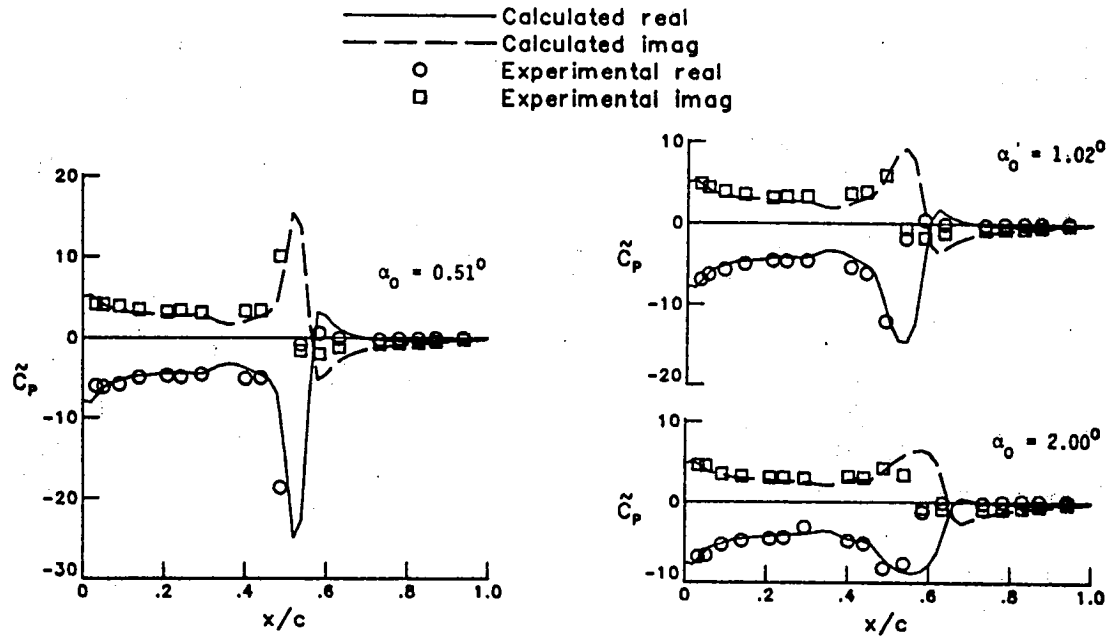

Figure 5. - Unsteady upper surface pressure distributions for the NACA 64A010A airfoil at M = 0.796, k = 0.1 (CT 8, 5, 9).

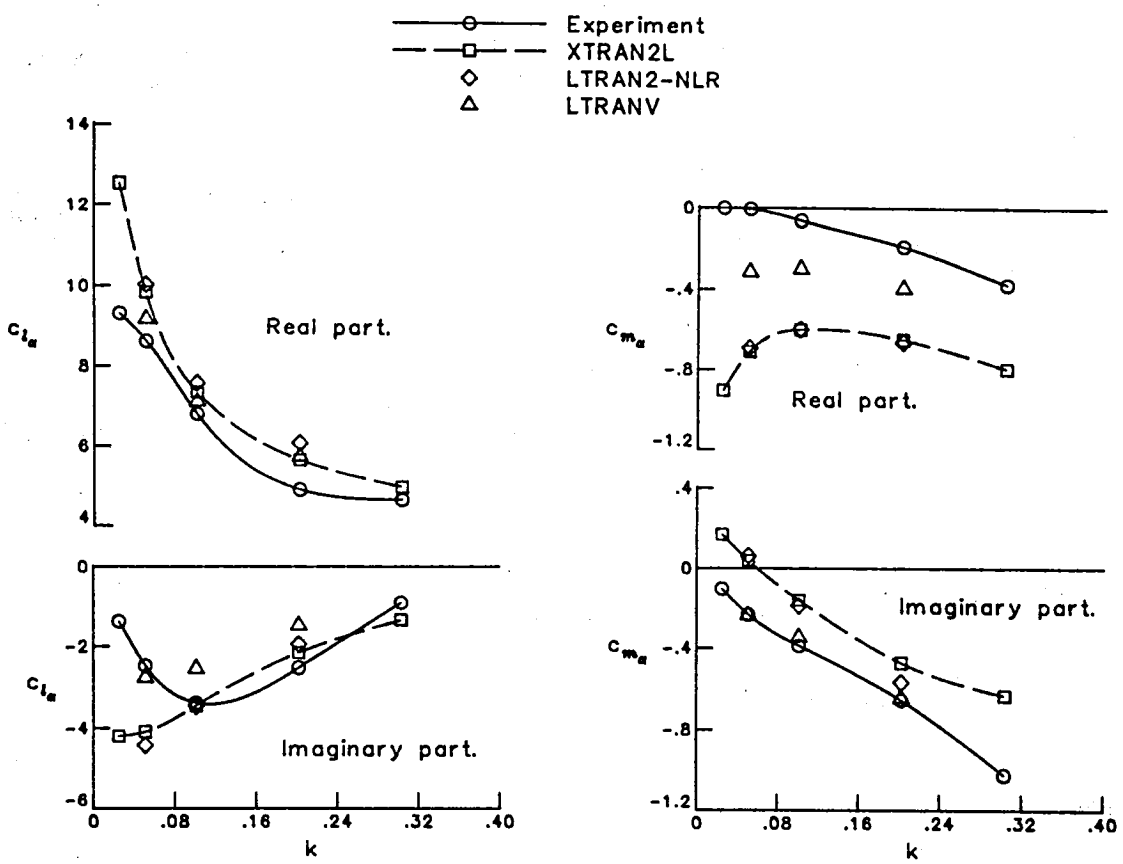

Figure 6. - Comparison of unsteady forces for the NACA 64A010A airfoil at M = 0.796, α_0 = 1° (CT 3-7).

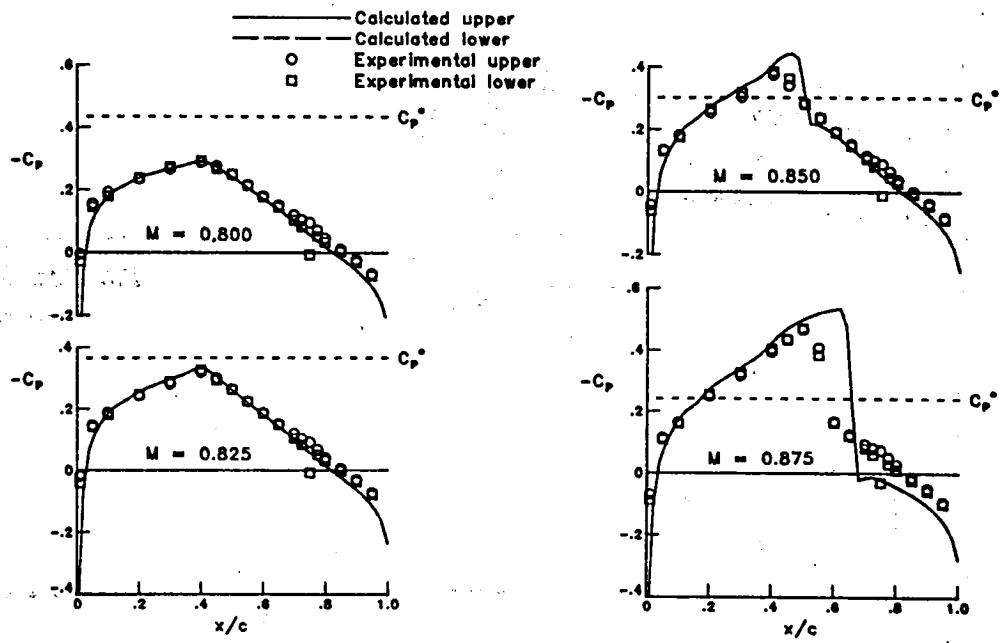

Figure 7. - Steady pressure distributions for the NACA 64A006 airfoil.

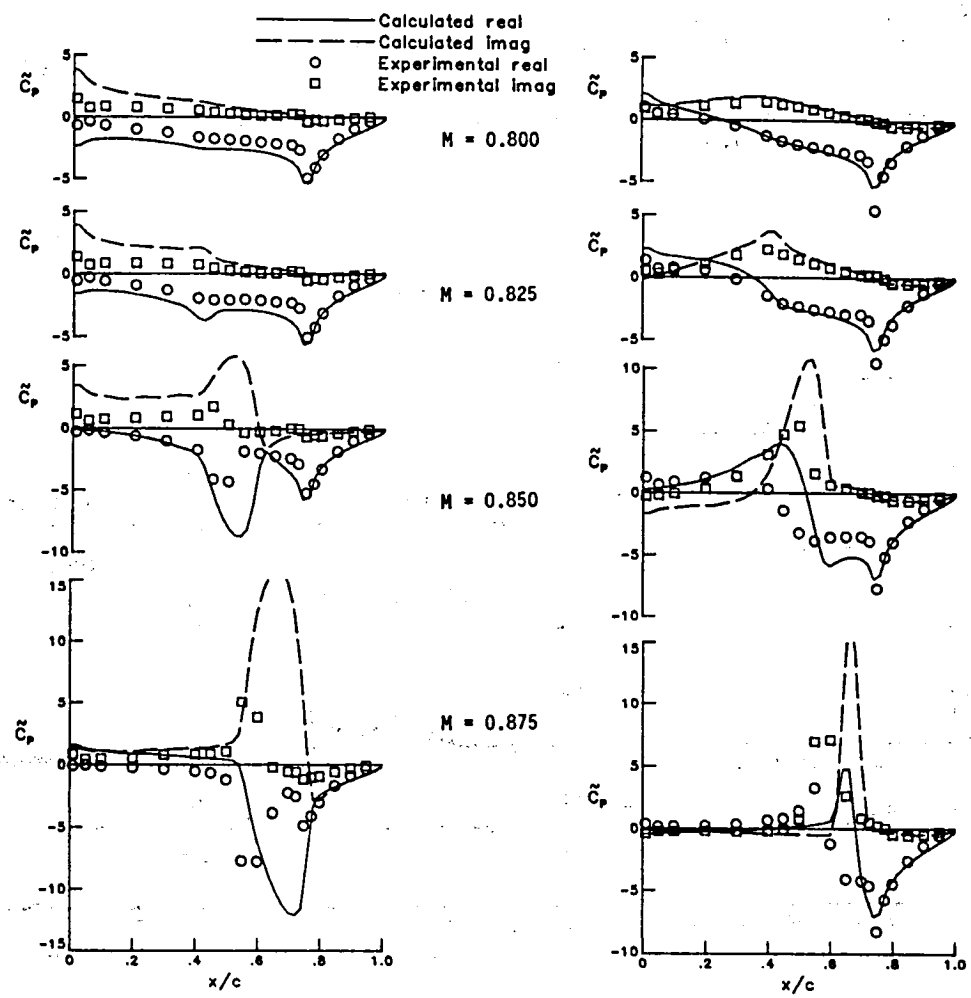

Figure 8. - Unsteady pressure distributions for the NACA 64A006 airfoil at $\delta_0 = 1^o$, k = 0.06 (CT 1, 3, 6, 8).

Figure 9. - Unsteady pressure distributions for the NACA 64A006 airfoil at $\delta_0 = 1^o$, k = 0.24 (CT 2, 5, 7, 10).

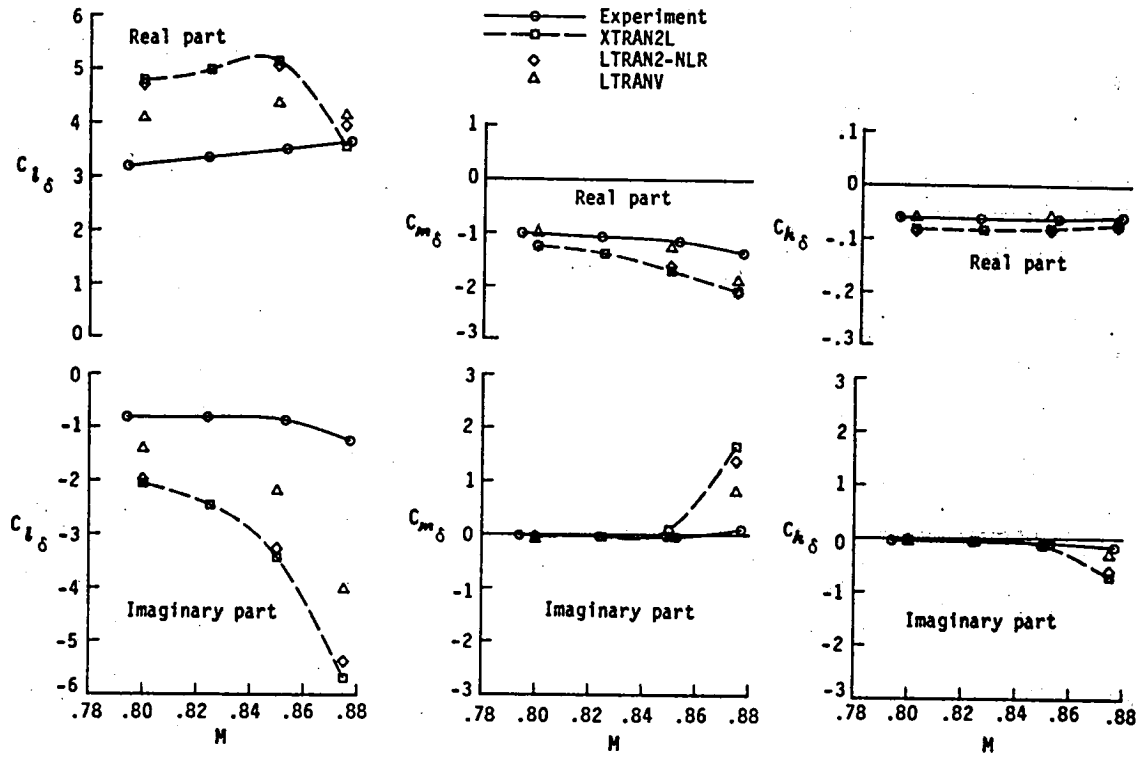

Figure 10. - Comparison of unsteady forces for the NACA 64A006 airfoil at $\delta_0 = 1^o$, k = 0.06 (CT 1, 3, 6, 8).

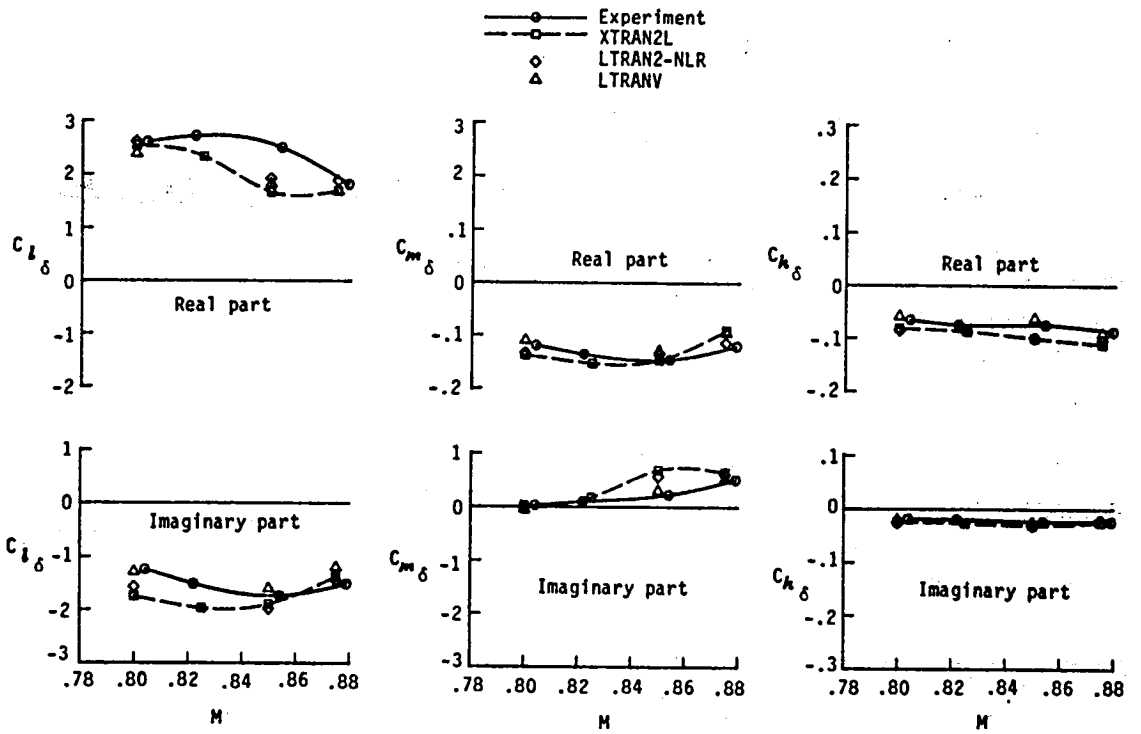

Figure 11. - Comparison of unsteady forces for the NACA 64A006 airfoil at $\delta_0 = 1^o$, k = 0.24 (CT 2, 5, 7, 10).

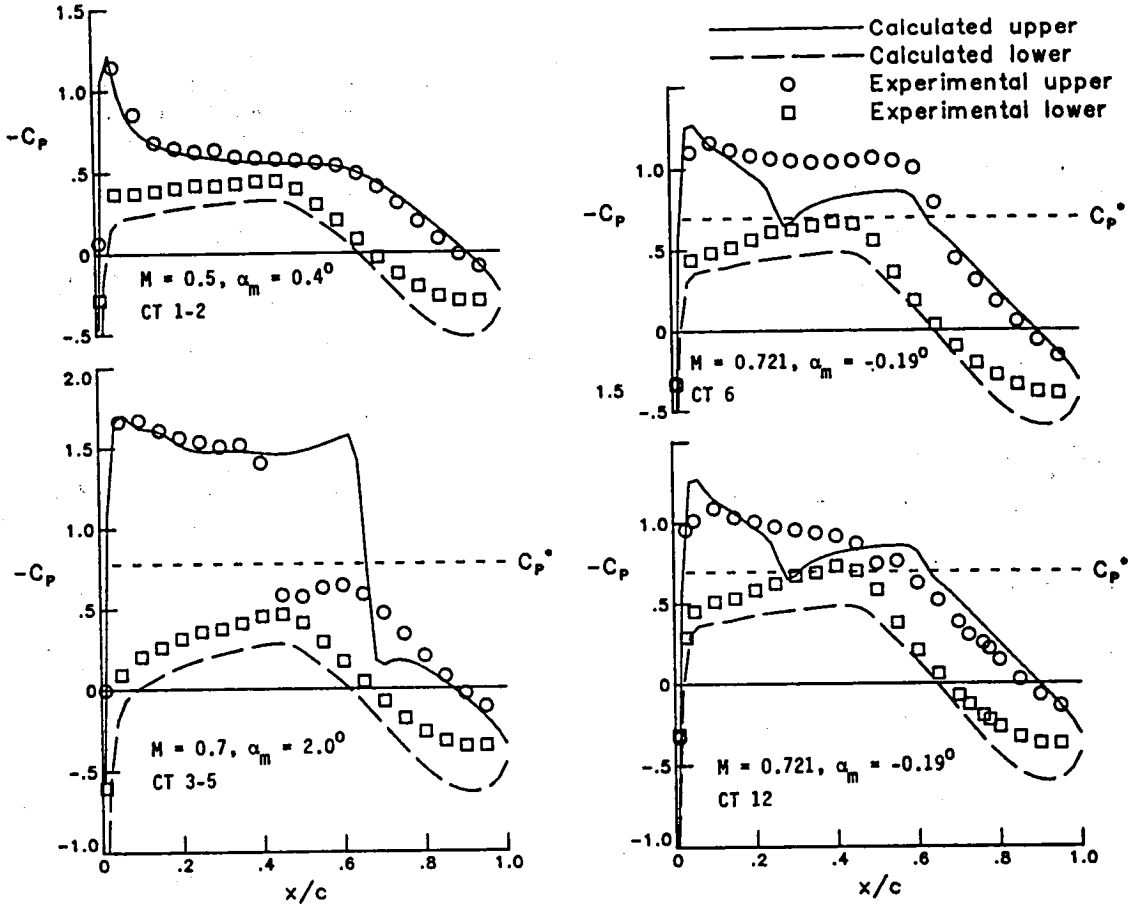

Figure 12. - Steady pressure distributions for the NLR 7301 airfoil.

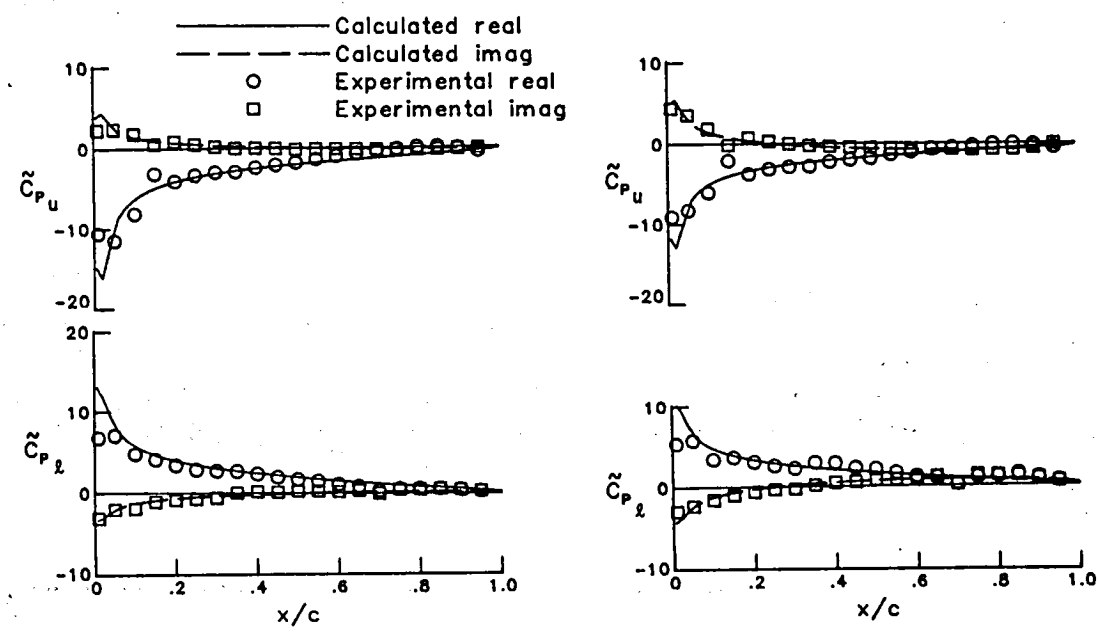

(a) k = 0.1 (CT 1)

(b) k = 0.263 (CT 2)

Figure 13. - Unsteady pressure distributions for the NLR 7301 airfoil at M = 0.5, α_m = 0.4°, α_0 = 0.5° (CT 1, 2).

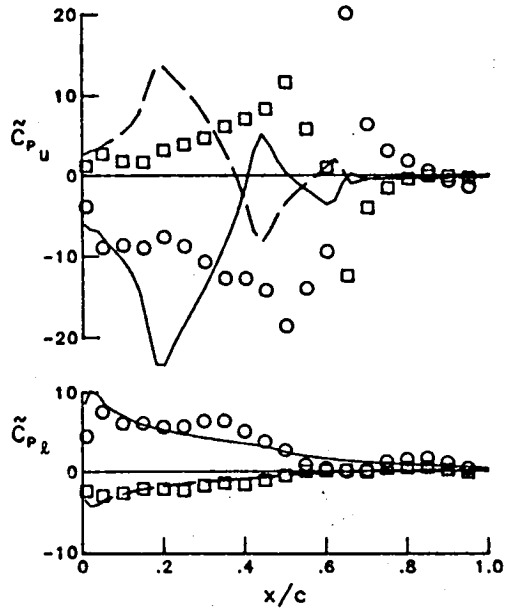

Figure 14. - Unsteady pressure distributions for the NLR 7301 airfoil at M = 0.721, α_m = -0.19°, α_0 = 0.5°, k = 0.068 (CT 6).

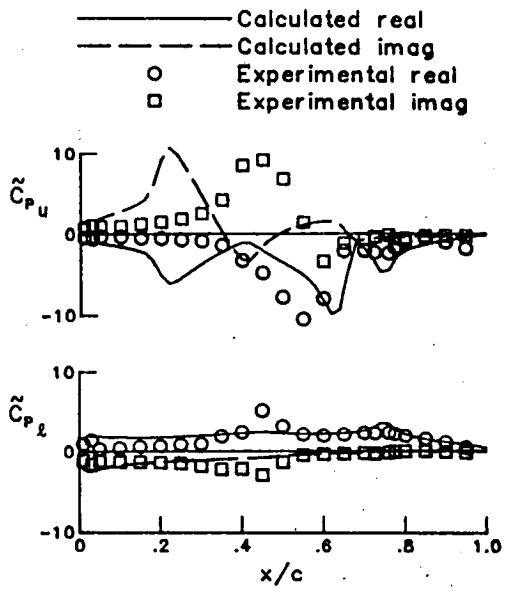

Figure 15. - Unsteady pressure distributions for the NLR 7301 airfoil at M = 0.721, α_m = -0.19°, δ_0 = 1°, k = 0.068 (CT 12).

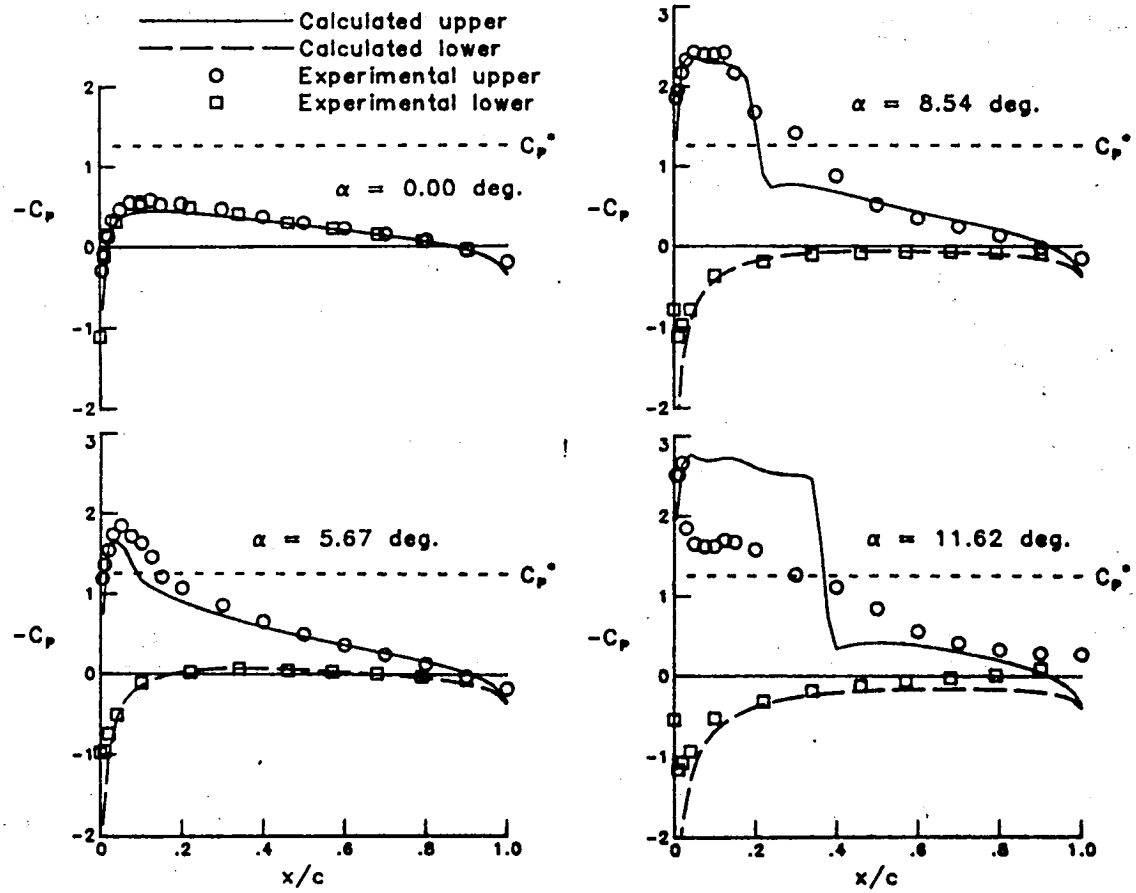

Figure 16. - Unsteady pressure distributions for the NACA 0012 airfoil during transient angle of attack change at M = 0.606 (CT 8).

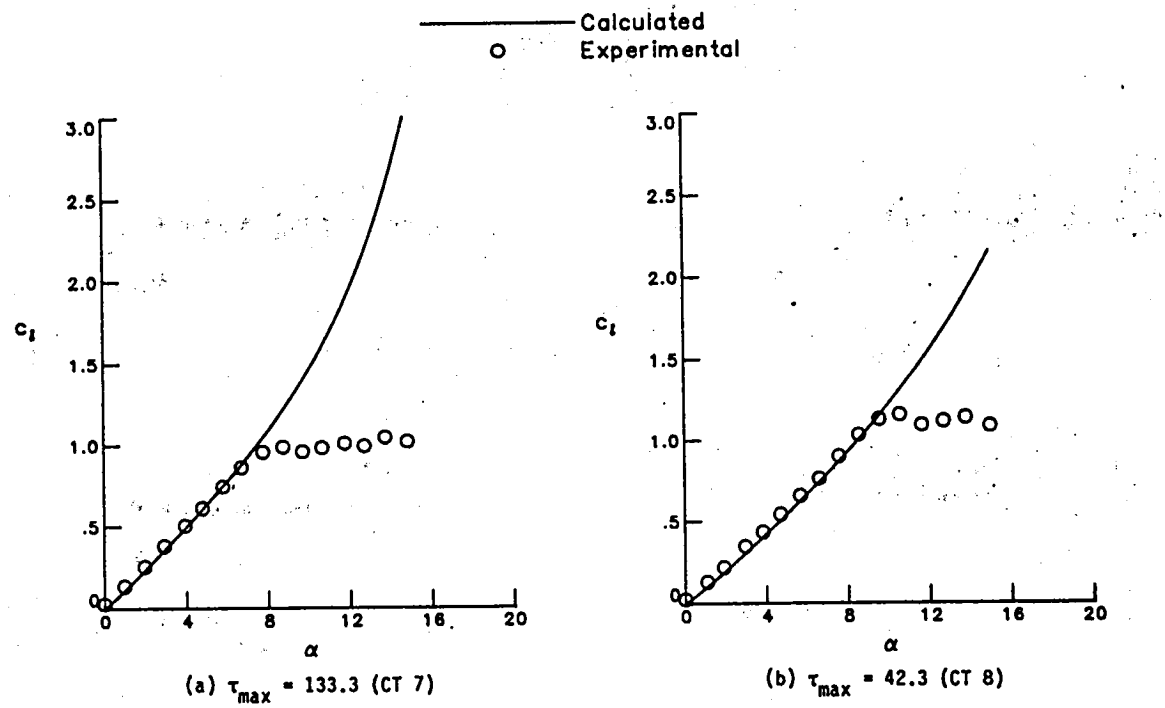

Figure 17. - Unsteady lift coefficients for the NACA 0012 airfoil during transient angle of attack changes at M = 0.6 (CT 7-8).

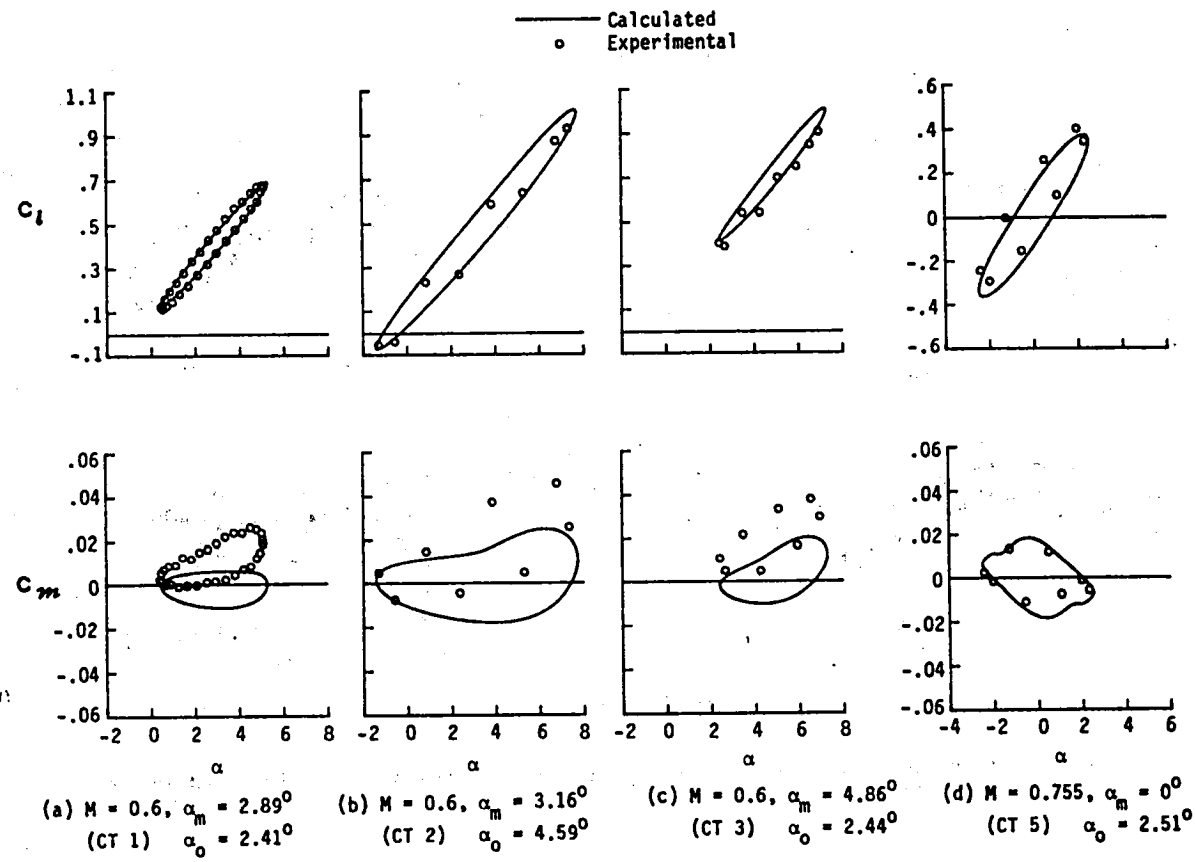

Figure 18. - Comparison of unsteady forces for the NACA 0012 at k = 0.081 (CT 1-3, 5).

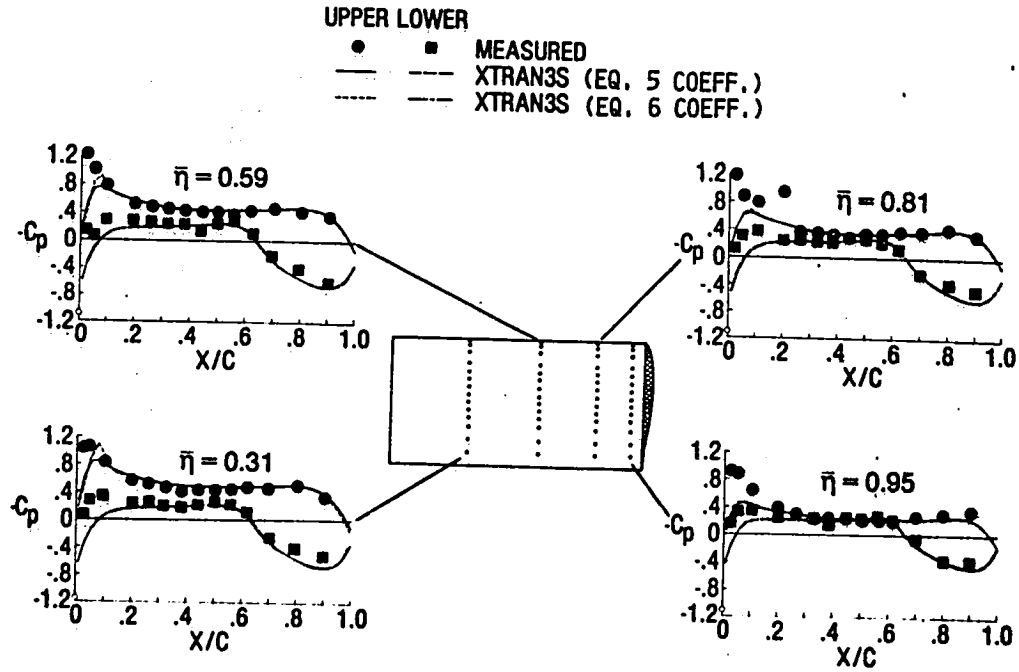

(a) M = 0.700

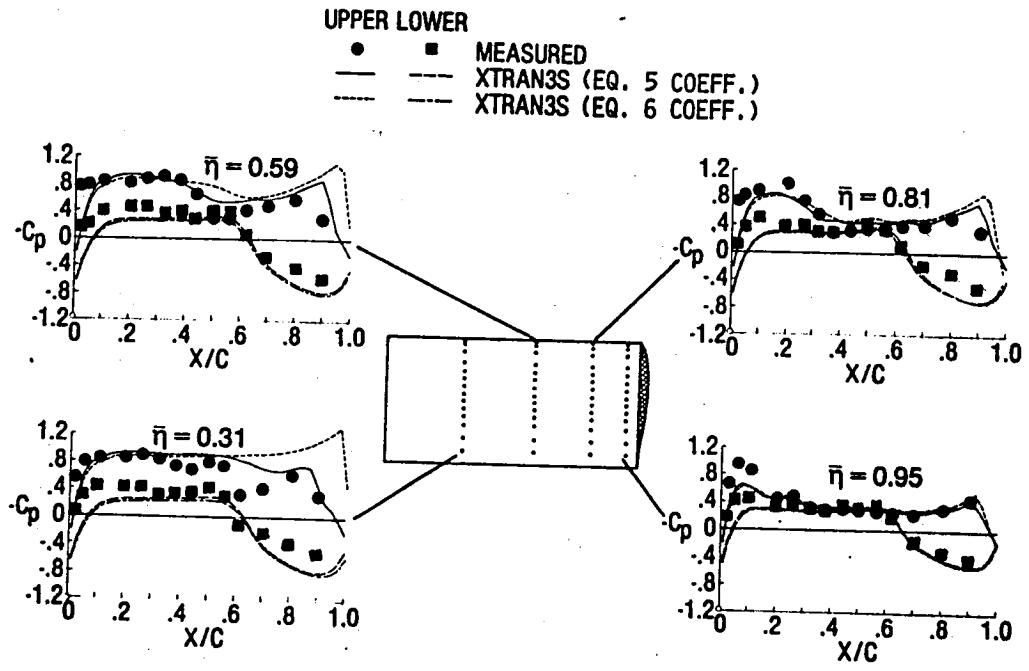

(b) M = 0.825

Figure 19. - Comparison of measured and calculated steady pressure distributions for rectangular supercritical wing at $\alpha_m = 2^0$.

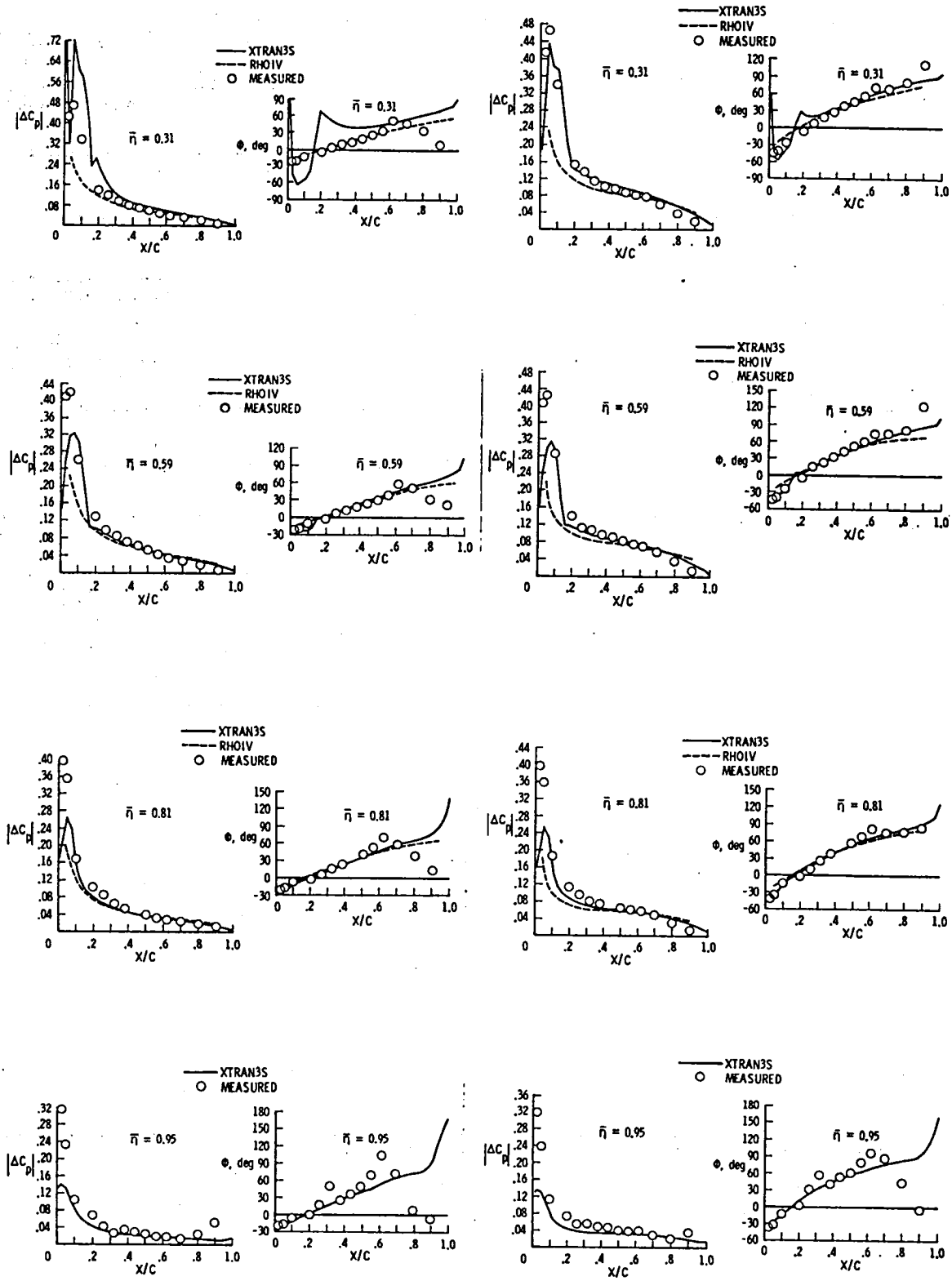

(a) k = 0.178

(b) k = 0.356

Figure 20. - Comparison of measured and calculated unsteady pressure distributions for rectangular supercritical wing at M = 0.7, $\alpha_m = 2^o$, $\alpha_o = 1^o$.

1. Report No.	2. Government Accession No.	3. Recipient's Catalog No.
NASA TM-86278		

4. Title and Subtitle	5. Report Date
EXPERIENCE WITH TRANSONIC UNSTEADY AERODYNAMIC CALCULATIONS	August 1984
	6. Performing Organization Code 505-33-43-09

7. Author(s)	8. Performing Organization Report No.
J. W. Edwards, S. R. Bland and D. A. Seidel	
	10. Work Unit No.

9. Performing Organization Name and Address	11. Contract or Grant No.
NASA Langley Research Center Hampton, VA 23665	
	13. Type of Report and Period Covered Technical Memorandum

12. Sponsoring Agency Name and Address	14. Sponsoring Agency Code
National Aeronautics and Space Administration Washington, DC 20546	505-33-43-09

15. Supplementary Notes

To be presented at the 59th Meeting of the AGARD Structures and Materials Panel, Specialists Meeting on Transonic Unsteady Aerodynamics and Its Aeroelastic Applications, Toulouse, France, September 2-7, 1984

16. Abstract

Comparisons of calculated and experimental transonic unsteady pressures and airloads for four of the AGARD Two-Dimensional Aeroelastic Configurations and for a rectangular supercritical wing are presented. The two-dimensional computer code, XTRAN2L, implementing the transonic small perturbation equation was used to obtain results for: (1) pitching oscillations of the NACA 64A010A, NLR 7301 and NACA 0012 airfoils, (2) flap oscillations for the NACA 64A006 and NLR 7301 airfoils, and (3) transient ramping motions for the NACA 0012 airfoil. Results from the three-dimensional code XTRAN3S are compared with data from a rectangular supercritical wing oscillating in pitch. These cases illustrate the conditions under which the transonic inviscid small perturbation equation provides reasonable predictions.

17. Key Words (Suggested by Author(s))	18. Distribution Statement
Transonic Unsteady Aerodynamics AGARD Configurations	Unclassified - Unlimited Subject Category - 02

19. Security Classif. (of this report)	20. Security Classif. (of this page)	21. No. of Pages	22. Price
Unclassified	Unclassified	22	A02